Functional architecture of motion direction in the mouse superior colliculus

Ya-tang Li[1], Zeynep Turan[1], and Markus Meister[1,2]

[1]Division of Biology and Biological Engineering, California Institute of Technology, Pasadena, CA 91125, USA

[2]Tianqiao and Chrissy Chen Institute for Neuroscience, California Institute of Technology, Pasadena, CA 91125, USA

Abstract

Motion vision is important in guiding animal behavior. Both the retina and the visual cortex process object motion in largely unbiased fashion: all directions are represented at all locations in the visual field. We investigate motion processing in the superior colliculus of the awake mouse, by optically recording neural responses across both hemispheres. Within the retinotopic map, one finds large regions of ~500 μm size where neurons prefer the same direction of motion. This preference is maintained in depth to ~350 μm. The scale of these patches, ~30 deg of visual angle, is much coarser than the animal's visual resolution. A global map of motion direction shows approximate symmetry between the left and right hemispheres and a net bias for upward-nasal motion in the upper visual field. Unlike other parts of the early visual system, the superior colliculus develops a locally biased representation of object motion.

Introduction

The connection between the ecology of natural scenes and the neurobiology of vision has been a topic of enduring interest. To first approximation natural scenes are translation-invariant, meaning that any given visual feature or event is equally likely to happen anywhere in the image. This principle predicts that the neural representation of visual images should be approximately uniform everywhere in the visual field. Closer inspection suggests some departures from translation invariance. The upper visual field is often occupied by sky, which differs in content from the lower visual field. Also animals direct their eyes to salient points in the scene, which selects for certain image features at the center of gaze.

The first station of the visual system seems to follow the principle of uniform coverage. In the mammalian retina, each of ~30 distinct types of retinal ganglion cells (RGCs) conveys information about a specific visual feature[1,2]. Each cell type tiles the entire retina in a "mosaic" arrangement, ensuring a representation of its special feature at every point in the visual space. The primary visual cortex continues this pattern. Individual neurons there are often tuned to one line orientation or motion direction, but all the possible orientations and directions are represented at every point, or at least within 1-4 degrees of visual angle[3–9],[10].

An evolutionarily older visual pathway leads from the retina to the superior colliculus. In the superior colliculus the principle of uniform coverage appears to be broken. Some of the earliest recordings in cat and rabbit already suggested a preference for visual motion in specific directions depending on location in the visual field[11,12]. In mouse superior colliculus one finds large regions of the visual field, ~30° across, where neurons prefer stimuli with a specific line orientation[13–16]. Whether the representation of visual motion is

51 similarly biased in a coarse map remains debated[13,17,18]. Most of the studies to date were
52 performed in anesthetized animals with an acute cortical lesion to uncover the underlying
53 superior colliculus. Both of these perturbations are known to affect direction-selectivity of
54 neurons in the superior colliculus[16,19,20].

55 The goal of the present work is to reveal how the direction of visual motion is
56 represented in the superior colliculus of awake mice at a large-scale population level. To
57 this end, we applied two complementary approaches. Two-photon calcium imaging was
58 used to record neuronal responses at single-cell resolution in the posterior-medial SC of
59 behaving mice, leaving the cortex intact. To reveal the functional organization on a larger
60 scale over both hemispheres we applied a wide-field imaging method in an acortical mutant
61 mouse.

62 Results

63 Single-cell imaging reveals a coarse map for direction of motion

64 To investigate the tuning of SC neurons to the direction of motion, we imaged neuronal
65 calcium responses to dots and bars moving in different directions using two-photon
66 microscopy in awake mice (Fig. 1a). To maintain the integrity of the overlying cortex, one
67 is limited to the posterior-medial sector of the mouse SC that corresponds to the upper
68 lateral visual field[14] (Fig. 1b-c). Direction-selective (DS) SC neurons in this region
69 responded robustly to both moving dots and moving bars with a strong direction preference
70 (Fig. 1d). We defined an index of direction selectivity (DSI, see Methods) and focused
71 further analysis on neurons with DSI larger than 0.1 (Fig. 1e-f). Among these cells, the
72 response to preferred direction motion was ~3 times larger on average than that to the null
73 direction.

The moving-bar stimulus will drive feature detectors that are tuned to either motion direction or line orientation, leading to possible confounds, whereas a field of moving dots has no orientation signal. Therefore, we focused on results from moving dot stimuli. Figure 2 illustrates the direction tuning of neurons in the left posterior-medial SC of three different animals. In each case, neurons located near each other tend to have the same preferred direction of motion. That preferred direction varies only gradually across the surface of the SC (Fig. 2a-d), or remains constant over distances of several 100 µm (Figs 2e-h, 2i-l). At times, neurons that prefer two opposite directions are intermingled (Fig. 2i-l). None of these arrangements of preferred direction resembles the salt-and-pepper organization in rodent primary visual cortex (V1)[10] (see more examples in Supplementary Fig. 1). Instead, the preferred direction changes only slowly with the location on the SC, if at all. The regions of constant direction bias range ~500 µm in size, which corresponds to ~30 degrees of visual angle or 4 receptive-field diameters. Furthermore, in all 3 animals the preferred direction is the same, suggesting that the posterior-medial SC has a systematic bias for upward-nasal image motion.

To summarize the results across many recordings, we calculated for each field of neurons both a measure of the local scatter of preferred directions as well as the systematic gradient in the spatial map of preferred direction (Fig. 2m). The resulting distribution diverged dramatically from the null model in which each cell has an independent preferred direction (Fig. 2m). In more than half of the cases the preferred direction showed a bimodal distribution (Fig. 2n). Across all samples, the preferred direction was strongly biased towards ~220° (upward/nasal) (Fig. 2o). This biased representation of motion direction was also observed in the responses to moving bars (Supplementary Fig. 2).

97 To explore the organization of preferred direction in the vertical dimension, we imaged
98 neuronal responses up to ~350 µm deep in steps of 20-30 µm. We projected the direction
99 maps from different depths onto the same plane (Fig. 3a). This revealed that neurons with
100 short horizontal separation preferred a similar direction independent of depth (Fig. 3a-b).
101 Further analysis over 11 animals confirmed that preferred direction has a columnar
102 organization, in that it varies little in the vertical dimension (Fig. 3c).

103 **The preferred direction is orthogonal to the preferred orientation**

104 Early work on monkey and cat visual cortex discovered an orthogonal relationship
105 between preferred orientation and preferred direction[6,21]. We examine whether this claim
106 can be generalized to the mouse SC. To probe these two maps independently, we measured
107 the direction preference with moving dots that carry no orientation signal and the
108 orientation preference with flashed gratings that carry no motion signal (Fig. 4a). Analysis
109 of direction- and orientation-selective neurons in an entire window of cells spanning 580
110 µm revealed that the angle between their preferred direction and preferred orientation is
111 about 90° (Fig. 4b-c, Supplementary Fig. 3a-b). The orthogonal relationship was confirmed
112 by histogramming the difference between preferred direction and orientation for neurons
113 across many animals (Fig. 4d, 532 neurons from 14 animals).

114 **Wide-field imaging reveals the direction maps of two entire hemispheres**

115 The bias in the preferred direction towards upward motion among neurons in the
116 posterior-medial SC (see Fig. 2o) motivated us to explore the functional organization of
117 motion direction on a larger scale. To this end, we recorded from the entire SC using a
118 wide-field imaging technique that sacrifices single-cell resolution but promised a global
119 view of the gradual variations in direction tuning. We first validated the approach by

120 imaging responses in the same brain using both two-photon and wide-field microscopy.
121 Figure 5a-b illustrates the direction map in the posterior-medial segment of the SC obtained
122 by both techniques, with very similar results. For broader coverage, we imaged the SC of
123 mutant mice whose cortex remains undeveloped[22], leaving almost the entire SC directly
124 accessible for optical recording. By repeatedly moving the narrow window of the 2-photon
125 microscope, we accumulated single-cell recordings of the preferred motion direction for
126 ~600 neurons over much of the collicular surface (Fig. 5c-d). A subsequent repeat of the
127 same stimuli using the wide-field microscope yielded essentially the same map of preferred
128 direction (Fig. 5e). Furthermore, the direction map in the posterior-medial segment is the
129 same in cortex-less mutant and normal animals (compare to Fig. 5a-b). These results show
130 that wide-field imaging is a promising approach to reveal the functional organization of
131 direction preference at a large scale.

132 The patchy anatomy of preferred direction on the SC suggests that large parts of the
133 visual field experience a bias for certain motion directions. To investigate this functional
134 map, one needs to represent each neuron at the location of its receptive field, along with its
135 direction preference in visual field coordinates. The need to represent motion directions
136 throughout the entire visual field brings up an interesting challenge for graphic display.
137 The conventional spherical coordinate system for visual space has singularities at the
138 "north" and "south" poles (elevation = +90° and -90°) where the direction of motion cannot
139 be expressed with respect to the coordinates (at the North Pole all directions point south).
140 But the north pole of the spherical coordinate system is well within the visual field of the
141 mouse[23]. To eliminate these pathologies, we chose to represent the sphere with a "unipolar"
142 coordinate system that has only one singularity. That special point can be placed dead

behind the animal, outside of the visual field (Fig. 6a, Supplementary Fig. 4, see **Methods**). In the following, we will use these unipolar coordinates for large-scale maps of the mouse visual field.

For the sample recording of Fig. 5c we mapped the receptive fields and preferred directions of all neurons into visual space (Fig. 6b). As predicted, the preferred direction varies with location in the visual field. Patches of approximately constant bias, ranging from 10° to 40° in size, are separated by regions with sharp changes. The gradient of preferred direction varies across the visual space. Wide-field imaging performed across both sides of the brain confirmed the patchy organization and the net bias for upward motion. Furthermore, neurons representing the left and right visual fields appear to prefer mirror-symmetric directions (Fig. 6c, Supplementary Fig. 5).

To identify the systematic aspects of direction-sensitivity, we analyzed these global maps across many animals. The simplest overarching feature is the overall bias for certain directions of motion, slightly nasal of upward, which is mirror-symmetric across the two sides of the visual field (Fig. 7a). To quantify the size of the patches of constant direction, we calculated the autocorrelation function for each map, which yielded a full width at half maximum of 30° (Fig. 7b, Supplementary Fig. 6a). As might be expected this patch size is the same in the left and right half of the SC (Fig. 7c). The direction patterns in left and right visual fields do not align perfectly: A cross-correlation between the two sides has a somewhat wider peak of ~40° (Fig. 7c). This concordance is similar to that observed across different animals (Fig. 7c, Supplementary Fig. 6b-c).

One possible interpretation of the global inhomogeneity is that it relates somehow to the optic flow pattern created by self-motion of the animal. To evaluate this notion, we

compared the experimental preferred-direction maps to optic flow maps predicted from the six basic modes of self-motion (Supplementary Fig. 7). By projecting the optic flow map onto the direction map one gains an estimate of how strongly the stimulus activates the superior colliculus. For those self-motions without a lateral component, the two sides of the SC are tuned in the same way. In particular, they are more strongly activated by forward translation, down translation, and downward pitch (Fig. 7d). For those motions with a lateral component, the two sides are tuned in the opposite way. In particular, the left SC prefers translation to the right, clockwise roll, and yaw to the right; *vice versa* for the right SC. Most of these biases are highly significant and consistent across animals.

Discussion

This study extends our understanding of the functional architecture of visual features in the brain. We showed that the mouse superior colliculus represents visual motion with a bias that depends on location in the visual field. Nearby neurons prefer a similar direction of motion even over distances of ~500 μm on the collicular surface, corresponding to ~30 degrees of visual angle (Fig. 2). The direction bias extends vertically over several 100 μm to form columns of preferred direction (Fig. 3). For neurons that are selective both for direction and orientation, the preferred direction is orthogonal to the preferred orientation (Fig. 4). Large-scale wide-field imaging revealed a global map of preferred direction with coarse symmetry between two sides of the superior colliculus and a strong bias for upward-nasal motion in the upper visual field (Figs. 5–7). Here, we briefly discuss these conclusions and their implications.

187 **Relation to prior work**

188 Some of the features reported here have been described before: For example, de
189 Malmazet et al[17] report that nearby neurons in certain regions of the retinotopic map tend
190 to prefer the same direction of motion, and that this local preference also extends in depth.
191 There has been controversy on those points[16,18], but our results reliably confirm the
192 observation of a local direction bias. Building on this prior work, we here present a global
193 analysis of direction coding in the SC. We extend the measurements to a larger visual field,
194 especially in the superior elevations ignored in previous studies. We also record from both
195 sides of the brain, covering almost the entire surface of the SC accessible from above. We
196 established that the global map consists of multiple iso-direction patches and measured
197 their size. Furthermore, we assessed the symmetry of these patches across the two sides of
198 the SC and evaluated how the global direction map interacts with the global optic flow
199 fields that result from locomotion during natural behavior.

200 Our results differ from prior claims on the topic of orientation tuning and how it relates
201 to direction tuning. The present observation that preferred orientation systematically lies
202 perpendicular to the preferred direction is consistent with the relationship reported in
203 neurons of the visual cortex[5,6,21]. This contrasts with a prior report[17] which argued that
204 direction maps and orientation maps in mouse superior colliculus are independent. That
205 conclusion may have been affected by the choice of stimuli, which precluded an
206 independent measurement of orientation and direction tuning in the same neuron
207 (Supplementary Fig. 8). In the present study, tuning to line orientation vs object motion
208 was assessed by different stimulus probes.

209 **Functional anatomy in different species**

210 The functional organization of visual processing has been reported in the brains of
211 many species. The visual cortex of cat[10], monkey[6], and ferret[5] shows a functional map,
212 where a neuron's response features – such as preferred orientation and direction – depend
213 systematically on its location in the brain. In the rodent cortex there is less organization,
214 and neurons preferring different orientations are intermingled in a "salt-and-pepper"
215 pattern. Despite this difference, the common point is that neurons of all preferred
216 orientations (or directions) are represented within a visual region smaller than the receptive
217 field of a single neuron. In the primary visual cortex (V1) of the monkey, the orientation
218 columns measure about 0.1° on average, only one-tenth of the receptive field size[24]. In V1
219 of the tree shrew, all orientations are represented within a 4° visual angle, again smaller
220 than the average receptive field size[9]. By contrast, in the mouse superior colliculus, the
221 patches with uniform preferred orientation span ~30°, which greatly exceeds the RF size
222 of ~10°[16], or the visual acuity of 2°[14]. The results reported here show that the representation
223 of object motion in the superior colliculus is similarly dominated by such local biases. An
224 intriguing new feature is that the iso-direction patches contain a minority of neurons tuned
225 to the diametrically opposite direction (Fig. 2i,j,k,l). It will be important to understand the
226 relationship of these two neural populations within the local circuitry.

227 **How does the patchy direction map in the SC arise?**

228 Several explanations can be contemplated: (1) The local direction bias may exist already
229 in the neural projections from the retina. (2) It may result from selective connectivity
230 between the retinal inputs and the target neurons in the SC. (3) Or it may be constructed
231 by postsynaptic circuitry within the SC. It has been shown that much of the direction

232 selectivity in the mouse SC arises already in the excitatory synaptic inputs from retinal
233 ganglion cells[25], which argues for a diminished role of collicular interneurons in the
234 phenomenon. The mouse retina contains 8 types of direction-selective ganglion cells
235 (DSGCs). Their global distribution across the retina has been analyzed, and there is no
236 indication of local inhomogeneities that could explain the patchy organization in the
237 direction map of the SC[26–28]. Furthermore, the projections of DSGCs to the superficial SC
238 appear to form a layer of uniform density, with no indication that one subtype dominates
239 over the others in any local region[29,30]. This prior work suggests that each retinotopic
240 location on the SC receives an equally balanced input of direction-selective signals from
241 the retina, quite unlike what occurs in the optic tectum of the zebrafish[31]. If so, then the
242 local bias observed in iso-direction patches must result from selective connectivity between
243 SC neurons and specific subtypes of DSGCs, and that connectivity bias must somehow be
244 coordinated among nearby neurons. Conceivably the local circuitry of interneurons
245 contributes to this lateral coordination.

246 **Behavioral relevance**

247 Is there an intelligible purpose to the direction architecture in the mouse superior
248 colliculus? On a coarse scale, cells in the upper visual field systematically prefer motion in
249 the upward and nasal direction. Because activity in the upper visual field is generally
250 associated with defensive reactions[32,33], one may speculate that the direction tuning is
251 adapted to those functions. Note that an aerial predator approaching at a constant height
252 from the horizon will indeed follow an upward trajectory in the visual field that eventually
253 bends in a nasal direction towards the north pole, in line with the average direction tuning
254 of the SC (Supplementary Fig. 9).

In addition, the global bias in the upper visual field also predicts a selectivity for certain optic flows produced by self motion. For example, the superior colliculus as a whole should respond more strongly to forward motion of the animal than to backward motion, whereas horizontal turns left or right should produce excess activity in the right and left colliculus respectively. Such strong global signals may play a role in rapid feedback during the control of locomotion.

The other characteristic scale of the direction architecture is the smaller patches that deviate from the average tuning, measuring ~30° of visual angle in diameter. The meaning of these specializations is harder to discern. The effects are substantial: For a direction-selective neuron in such a patch, the median ratio between preferred and null direction response is about 2.2. Thus, differently tuned patches may differ by a factor of 4 in their relative response to two moving objects. This should produce noticeable regional gradients in the animal's perceptual sensitivity to motion, a prediction to be tested in future experiments.

Methods

Visual field coordinate systems. During experiments with visual stimulation, the animal was head-fixed with the lambda-bregma plane horizontal in the laboratory frame. To report locations in the visual field, we use either spherical coordinates $(\text{azimuth,elevation}) = (\varphi, \theta)$ or unipolar coordinates (α, β). The lambda-bregma plane is at $\theta = 0°$ and $\beta = 0°$.

Unipolar Coordinates. We introduce this coordinate system to avoid the singularities occurring at the poles of spherical coordinates. Suppose the observer sits at the origin of a Cartesian system facing in the *z*-direction. The horizontal plane is (x, z) and the *y*-axis points up. A unit sphere is centered on the origin. For a given point $\vec{r} = (x, y, z)$ on the sphere, spherical coordinates $(\text{azimuth,elevation}) = (\varphi, \theta)$ are defined as

$$\varphi = \arctan\frac{x}{z}, \theta = \arctan\frac{y}{z} \tag{1}$$

and unipolar coordinates (α, β) as

$$\alpha = 2\arctan\frac{x}{1+z}, \beta = 2\arctan\frac{y}{1+z} \tag{2}$$

Note the only singular point of the unipolar system is directly behind the observer at $\vec{r} = (0, 0, -1)$. The transformation from spherical coordinates to unipolar coordinates is:

$$\alpha = 2\arctan\frac{\cos\theta\sin\varphi}{1+\cos\theta\cos\varphi}, \beta = 2\arctan\frac{\sin\theta}{1+\cos\theta\cos\varphi} \tag{3}$$

The direction of motion on the sphere in unipolar coordinates is defined as

$$\rho = \arctan\frac{d\beta}{d\alpha} \tag{4}$$

where $d\alpha$ and $d\beta$ are increments of motion along α and β respectively.

Visual stimulation. For 2-photon imaging experiments, an LED screen was placed 15 cm away from the mouse's right eye. The center of the monitor was at 95° azimuth and 25° elevation in the laboratory frame, and the monitor covered a visual field of 106° x 79°. The monitor was strobed for 12 μs at the end of each laser scan line to minimize interference of the stimulus with fluorescence detection. For measuring neuronal tuning to orientation and motion direction we applied three types of stimuli. (1) A 2-d array of moving dots with a diameter of 5° spaced at 54°. The array moved in 12 possible directions. This stimulus contains no orientation signal. (2) Square gratings with a spatial frequency of 0.08 cycles per degree were flashed at 6 orientations and 4 phases. This stimulus contains no motion signal. (3) A moving dark bar with 5° width moving in 12 possible directions. The sequence of directions or orientations was pseudorandomized.

For the wide-field imaging setup, a large LED screen was placed 15 cm away from the mouse's eye covering a visual field of 145° x 121°. The center of the monitor was at 25° elevation and either 0° azimuth (covering both eyes), 45° azimuth (mostly right eye) or -45° azimuth (mostly left eye). To avoid excessive fisheye distortion in these wide-field experiments, we applied a spherical correction to the images on the monitor [34].

Viral injection. We injected adeno-associated virus (AAV) expressing non-floxed GCaMP6 (AAV2/1.hSyn1.GCaMP6f.WPRE.SV40) into the SC of C57BL/6J and the SC of mutant mice with the largely undeveloped cortex. After 2–3 weeks, we implanted a cranial window coupled to a transparent silicone plug that rested on the surface of the SC and exposed its caudomedial portion. This portion of the SC corresponds to the up-temporal part of the visual field. The optics remained clear for several months, which enabled long-

312 term monitoring of the same neurons. Two-photon microscopy was applied to image
313 calcium signals in the SC of head-fixed awake mice 3 weeks to 2 months after viral injection.

314 **2-photon calcium imaging and analysis.**

315 Two-photon imaging was performed on a custom-built microscope with a 16×, 0.8 NA,
316 3mm WD objective (Nikon) and controlled by custom software written in Labview
317 (National Instruments). A Ti:Sapphire laser with mode-locking technique (Spectra-Physics
318 Mai Tai HP DeepSee) was scanned by galvanometers (Cambridge). GCaMP6f was excited
319 at 920 nm and laser power at the sample plane was typically 20-80 mW. A 600 μm × 600
320 μm field of view was scanned at 4.8 Hz as a series of 250 pixel × 250 pixel images and the
321 imaging depth was up to 350 μm. Emitted light was collected with a T600/200dcrb dichroic
322 (Chroma), passed through a HQ575/250m-2p bandpass filter (Chroma), and detected by a
323 photomultiplier tube (R3896, Hamamatsu). Artifacts of the strobed stimulus were
324 eliminated by discarding 8 pixels on either end of each line.

325 Brain motion during imaging was corrected using SIMA[35] or NoRMCorre[36]. Regions
326 of interest (ROIs) were drawn manually using Cell Magic Wand Tool (ImageJ) and fitted
327 with an ellipse in Matlab. Fluorescence traces of each ROI were extracted after estimating
328 and removing contamination from surrounding neuropil signals as described previously[14,37].
329 Slow baseline fluctuations were removed by subtracting the eighth percentile value from a
330 15-s window centered on each frame[38].

331 Two criteria were applied to interpret ROIs as neurons: 1) The size of ROI was limited
332 to 10 – 20 μm to match the size of a neuron; 2) ROIs with a signal-to-noise ratio (SNR)
333 smaller than 0.4 were discarded from further analysis[39].

$$SNR = \frac{Var\left[\langle C \rangle_r\right]_t}{\left\langle Var\left[C\right]_t \right\rangle_r} \tag{5}$$

Where C is the $T \times R$ response matrix (time samples × stimulus repetitions), $\langle\ \rangle$ and $Var[\ ]$ is the mean and variance.

For any given stimulus, the response of a neuron was defined by the fluorescence trace in its ROI during the stimulus period

$$R = \frac{\text{peak fluorescence - baseline}}{\text{baseline}} \tag{6}$$

where the baseline is derived from a 0.5-s period prior to stimulation.

To quantify the tuning of a neuron to motion direction, we computed the preferred direction as the argument of the response-weighted vector sum of all directions:

$$\rho_{pref} = \arg(\sum_k R(\rho_k) \times e^{i\rho_k}) \tag{7}$$

where $R(\rho_k)$ is the response amplitude at the kth direction ρ_k. The direction selectivity index (DSI) was calculated as the normalized amplitude of the sum:

$$DSI = \frac{\left|\sum_k R(\rho_k) \times e^{i\rho_k}\right|}{\sum_k R(\rho_k)} \tag{8}$$

Similarly, for orientation tuning, the preferred orientation was calculated as the argument of the response-weighted vector sum of all orientations:

$$\theta_{pref} = \arg(\sum_k R(\theta_k) \times e^{2i\theta_k}) \tag{9}$$

where $R(\theta_k)$ is the response amplitude at the kth orientation θ_k. The orientation selectivity index (OSI) was calculated as the normalized amplitude of the sum:

$$OSI = \frac{\left|\sum_k R(\theta_k) \times e^{2i\theta_k}\right|}{\sum_k R(\theta_k)} \tag{10}$$

We assessed the statistical significance of DSI and OSI using a permutation test[40]: Surrogate trials were generated by randomly shuffling the trial labels and recomputing the DSI or OSI. This procedure was repeated 1000 times to generate a null distribution. Neurons were classified as direction-selective if $DSI > 0.1$ and $p < 0.05$, and as orientation-selective if $OSI > 0.1$ and $p < 0.05$.

The direction map was generated by linearly interpolating the single-cell-resolution data and then applying a mean filter over a 200-μm square region. To calculate the gradient of the map, the map of the preferred direction was fitted by:

$$\rho(x, y) = dx \times x + dy \times y + b \tag{11}$$

where x and y are the anatomical coordinates. The gradient was calculated as:

$$gradient = \sqrt{dx^2 + dy^2} \tag{12}$$

The artificial random arrangement of preferred direction (Fig. 2m) was simulated as 26×26 neurons, each of which prefers a random direction, evenly distributed on a $500\mu m \times 500\mu m$ anatomy space.

To find the optimal number of Gaussians to fit the preferred direction distribution (Fig. 2n), we evaluated the Bayesian information criterion (BIC)[41]:

$$BIC = -2 \log L + M \log N \tag{13}$$

where L is the maximized likelihood, M is the number of parameters in the model, and N is the number of neurons.

The center of the receptive field (RF) of each neuron was calculated based on the moving-bar responses. For each direction of motion, the time of peak response depends on the location of the RF and the neuron's response latency. By evaluating responses to all directions, one can extract the response latency and determine the best-fit location of the RF.

Wide-field imaging and analysis. The wide-field microscope was built with a 50-mm / 105-mm tandem lens[42]. Illumination was from a blue LED with an excitation filter (469 nm ± 35 nm) and the camera used an emission filter (525 nm ± 39 nm). Images were acquired using a CMOS camera (Basler ace acA2000-165um NIR USB 3.0 Camera) at an acquisition rate of 10 Hz. The camera covers an area of 5.36 mm x 2.85 mm at a spatial resolution of 2.63 μm. Each acquired image was convolved with a normalized box filter and down-sampled to 1/10 of the original size. An ROI was drawn manually over the SC to exclude signals from the surrounding areas. For each pixel in the image, the response was defined as described above for ROIs in 2-photon experiments. The RF center of each pixel was calculated from moving bar responses as described above.

To measure the size of direction-tuned patches in a direction map, we calculated the normalized 2-D autocorrelation of the map. Similarly to evaluate the correspondence between maps on the left and right SC or across different mice, we calculated the normalized 2-D cross-correlation of two maps. Suppose a direction map is given by $\vec{u}(\mathbf{x})$, where at each location $\mathbf{x}$ in the visual field $\vec{u}(\mathbf{x})$ is a vector that points in the preferred direction ρ with length proportional to the DSI. For two such direction maps $\vec{u}(\mathbf{x})$ and $\vec{v}(\mathbf{x})$ we define the cosine correlation as

$$c(\mathbf{y}) = \frac{\int \vec{u}(\mathbf{x}) \cdot \vec{v}(\mathbf{x}+\mathbf{y}) \mathrm{d}^2 x}{\sqrt{\int \vec{u}(\mathbf{x}) \cdot \vec{u}(\mathbf{x}) \mathrm{d}^2 x \int \vec{v}(\mathbf{x}) \cdot \vec{v}(\mathbf{x}) \mathrm{d}^2 x}} \tag{14}$$

For every possible shift vector **y** this computes the normalized dot product of one map with the shifted version of the other map. We averaged this correlation map over all shift vectors of the same distance $|y| = r$ to obtain a radial profile $C(r)$. The full width at half maximum (FWHM) of the correlation map (Fig. 7) was defined as twice the radius where this profile dropped to half of its maximum.

Statistical methods. No statistical method was used to predetermine the sample size. A permutation test was used to assess the statistical significance of DSI and OSI as described above. The Shapiro-Wilk test was applied to assess whether data were normally distributed. In the case of a normal distribution, a *t*-test was applied; otherwise, a nonparametric test (Mann–Whitney U-test or One-sample Wilcoxon signed-rank test) was applied.

Acknowledgments M.M was supported by a grant from NIH (R01 NS111477). Y.L.was supported by NEI K99EY028640 and a Helen Hay Whitney Postdoctoral Fellowship.

Author Contributions Y.L. designed the study, performed all experiments, interpreted results, and wrote the manuscript. Z.T. provided acortical mutant mice and validated their brain anatomy. M.M. helped design the study, interpret results, and write the manuscript.

Author Information Correspondence and requests for materials should be addressed to M.M. (meister@caltech.edu) or Y.L. (yatangli8@gmail.com).

Competing interests statement The authors declare no competing financial interests.

417 ## Reference

418 1. Roska, B. & Meister, M. The retina dissects the visual scene into distinct features.
419 *New Vis. Neurosci.* 163–82 (2014).
420 2. Sanes, J. R. & Masland, R. H. The Types of Retinal Ganglion Cells: Current Status
421 and Implications for Neuronal Classification. *Annu. Rev. Neurosci.* **38,** 221–246
422 (2015).
423 3. Blasdel, G. G. & Salama, G. Voltage-sensitive dyes reveal a modular organization in
424 monkey striate cortex. *Nature* **321,** 579–585 (1986).
425 4. Bonhoeffer, T. & Grinvald, A. Iso-orientation domains in cat visual cortex are
426 arranged in pinwheel-like patterns. *Nature* **353,** 429–431 (1991).
427 5. Weliky, M., Bosking, W. H. & Fitzpatrick, D. A systematic map of direction
428 preference in primary visual cortex. *Nature* **379,** 725–728 (1996).
429 6. Malonek, D., Tootell, R. B. H. & Grinvald, A. Optical imaging reveals the functional
430 architecture of neurons processing shape and motion in owl monkey area MT. *Proc R*
431 *Soc Lond B* **258,** 109–119 (1994).
432 7. Tusa, R. J., Rosenquist, A. C. & Palmer, L. A. Retinotopic organization of areas 18
433 and 19 in the cat. *J. Comp. Neurol.* (1979). doi:10.1002/cne.901850405
434 8. Law, M. I., Zahs, K. R. & Stryker, M. P. Organization of primary visual cortex (area
435 17) in the ferret. *J. Comp. Neurol.* **278,** 157–180 (1988).
436 9. Bosking, W. H., Crowley, J. C. & Fitzpatrick, D. Spatial coding of position and
437 orientation in primary visual cortex. *Nat. Neurosci.* **5,** 874–882 (2002).

10. Ohki, K., Chung, S., Ch'ng, Y. H., Kara, P. & Reid, R. C. Functional imaging with cellular resolution reveals precise micro-architecture in visual cortex. *Nature* **433,** 597 (2005).
11. Schaefer, K.-P. Mikroableitungen im Tectum opticum des frei beweglichen Kaninchens. *Arch. Für Psychiatr. Nervenkrankh.* **208,** 120–146 (1966).
12. Straschill, M. & Hoffmann, K. P. Functional aspects of localization in the cat's tectum opticum. *Brain Res.* **13,** 274–283 (1969).
13. Ahmadlou, M. & Heimel, J. A. Preference for concentric orientations in the mouse superior colliculus. *Nat. Commun.* **6,** 6773 (2015).
14. Feinberg, E. H. & Meister, M. Orientation columns in the mouse superior colliculus. *Nature* **519,** 229–232 (2015).
15. Dräger, U. C. & Hubel, D. H. Responses to visual stimulation and relationship between visual, auditory, and somatosensory inputs in mouse superior colliculus. *J. Neurophysiol.* **38,** 690–713 (1975).
16. Wang, L., Sarnaik, R., Rangarajan, K., Liu, X. & Cang, J. Visual Receptive Field Properties of Neurons in the Superficial Superior Colliculus of the Mouse. *J. Neurosci.* **30,** 16573–16584 (2010).
17. de Malmazet, D., Kühn, N. K. & Farrow, K. Retinotopic Separation of Nasal and Temporal Motion Selectivity in the Mouse Superior Colliculus. *Curr. Biol.* (2018). doi:10.1016/j.cub.2018.07.001
18. Inayat, S., Barchini, J., Chen, H., Feng, L., Liu, X. & Cang, J. Neurons in the Most Superficial Lamina of the Mouse Superior Colliculus Are Highly Selective for Stimulus Direction. *J. Neurosci.* **35,** 7992–8003 (2015).

461 19. Rosenquist, A. C. & Palmer, L. A. Visual receptive field properties of cells of the
462 superior colliculus after cortical lesions in the cat. *Exp. Neurol.* **33,** 629–652 (1971).
463 20. Wickelgren, B. G. & Sterling, P. Influence of visual cortex on receptive fields in the
464 superior colliculus of the cat. *J. Neurophysiol.* **32,** 16–23 (1969).
465 21. Shmuel, A. & Grinvald, A. Functional Organization for Direction of Motion and Its
466 Relationship to Orientation Maps in Cat Area 18. *J. Neurosci.* **16,** 6945–6964 (1996).
467 22. Kim, S., Lehtinen, M. K., Sessa, A., Zappaterra, M. W., Cho, S.-H., Gonzalez, D.,
468 Boggan, B., Austin, C. A., Wijnholds, J., Gambello, M. J., Malicki, J., LaMantia, A.
469 S., Broccoli, V. & Walsh, C. A. The Apical Complex Couples Cell Fate and Cell
470 Survival to Cerebral Cortical Development. *Neuron* **66,** 69–84 (2010).
471 23. Sterratt, D. C., Lyngholm, D., Willshaw, D. J. & Thompson, I. D. Standard
472 Anatomical and Visual Space for the Mouse Retina: Computational Reconstruction
473 and Transformation of Flattened Retinae with the Retistruct Package. *PLoS Comput.*
474 *Biol.* **9,** e1002921 (2013).
475 24. Blasdel, G. & Campbell, D. Functional Retinotopy of Monkey Visual Cortex. *J.*
476 *Neurosci.* **21,** 8286–8301 (2001).
477 25. Shi, X., Barchini, J., Ledesma, H. A., Koren, D., Jin, Y., Liu, X., Wei, W. & Cang, J.
478 Retinal origin of direction selectivity in the superior colliculus. *Nat. Neurosci.* **20,**
479 550–558 (2017).
480 26. Sabbah, S., Gemmer, J. A., Bhatia-Lin, A., Manoff, G., Castro, G., Siegel, J. K.,
481 Jeffery, N. & Berson, D. M. A retinal code for motion along the gravitational and
482 body axes. *Nature* **546,** 492–497 (2017).

483 27. Kim, I.-J., Zhang, Y., Yamagata, M., Meister, M. & Sanes, J. R. Molecular
484 identification of a retinal cell type that responds to upward motion. *Nature* **452,** 478–
485 482 (2008).
486 28. Yonehara, K., Ishikane, H., Sakuta, H., Shintani, T., Nakamura-Yonehara, K.,
487 Kamiji, N. L., Usui, S. & Noda, M. Identification of Retinal Ganglion Cells and Their
488 Projections Involved in Central Transmission of Information about Upward and
489 Downward Image Motion. *PLOS ONE* **4,** e4320 (2009).
490 29. Huberman, A. D., Wei, W., Elstrott, J., Stafford, B. K., Feller, M. B. & Barres, B. A.
491 Genetic Identification of an On-Off Direction- Selective Retinal Ganglion Cell
492 Subtype Reveals a Layer-Specific Subcortical Map of Posterior Motion. *Neuron* **62,**
493 327–334 (2009).
494 30. Kay, J. N., Huerta, I. D. la, Kim, I.-J., Zhang, Y., Yamagata, M., Chu, M. W.,
495 Meister, M. & Sanes, J. R. Retinal Ganglion Cells with Distinct Directional
496 Preferences Differ in Molecular Identity, Structure, and Central Projections. *J.*
497 *Neurosci.* **31,** 7753–7762 (2011).
498 31. Nikolaou, N., Lowe, A. S., Walker, A. S., Abbas, F., Hunter, P. R., Thompson, I. D.
499 & Meyer, M. P. Parametric Functional Maps of Visual Inputs to the Tectum. *Neuron*
500 **76,** 317–324 (2012).
501 32. Dean, P., Mitchell, I. J. & Redgrave, P. Responses resembling defensive behaviour
502 produced by microinjection of glutamate into superior colliculus of rats.
503 *Neuroscience* **24,** 501–510 (1988).

33. Sahibzada, N., Dean, P. & Redgrave, P. Movements resembling orientation or avoidance elicited by electrical stimulation of the superior colliculus in rats. *J. Neurosci.* **6,** 723–733 (1986).
34. Marshel, J. H., Garrett, M. E., Nauhaus, I. & Callaway, E. M. Functional Specialization of Seven Mouse Visual Cortical Areas. *Neuron* **72,** 1040–1054 (2011).
35. Kaifosh, P., Zaremba, J. D., Danielson, N. B. & Losonczy, A. SIMA: Python software for analysis of dynamic fluorescence imaging data. *Front. Neuroinformatics* **8,** (2014).
36. Pnevmatikakis, E. A. & Giovannucci, A. NoRMCorre: An online algorithm for piecewise rigid motion correction of calcium imaging data. *J. Neurosci. Methods* **291,** 83–94 (2017).
37. Göbel, W. & Helmchen, F. In Vivo Calcium Imaging of Neural Network Function. *Physiology* **22,** 358–365 (2007).
38. Dombeck, D. A., Khabbaz, A. N., Collman, F., Adelman, T. L. & Tank, D. W. Imaging Large-Scale Neural Activity with Cellular Resolution in Awake, Mobile Mice. *Neuron* **56,** 43–57 (2007).
39. Baden, T., Berens, P., Franke, K., Román Rosón, M., Bethge, M. & Euler, T. The functional diversity of retinal ganglion cells in the mouse. *Nature* **529,** 345–350 (2016).
40. Ecker, A. S., Berens, P., Cotton, R. J., Subramaniyan, M., Denfield, G. H., Cadwell, C. R., Smirnakis, S. M., Bethge, M. & Tolias, A. S. State Dependence of Noise Correlations in Macaque Primary Visual Cortex. *Neuron* **82,** 235–248 (2014).
41. Kass, R. E. & Raftery, A. E. Bayes Factors. *J. Am. Stat. Assoc.* **90,** 773–795 (1995).

42. Ratzlaff, E. H. & Grinvald, A. A tandem-lens epifluorescence macroscope: Hundred-fold brightness advantage for wide-field imaging. *J. Neurosci. Methods* **36,** 127–137 (1991).

43. Oommen, B. S. & Stahl, J. S. Eye orientation during static tilts and its relationship to spontaneous head pitch in the laboratory mouse. *Brain Res.* **1193,** 57–66 (2008).

534 ## Figure Legends

535 **Figure 1 | Two-photon calcium imaging reveals direction tuning in awake mouse**
536 **superior colliculus. a**, Schematic of the experimental setup. Mice were head-fixed and
537 free to run on a circular treadmill. Visual stimuli were presented on a screen. Neuronal
538 calcium activity was imaged using two-photon microscopy. PMT, photomultiplier tube**. b**,
539 Schematic of mouse brain anatomy after insertion of a triangular plug to reveal the
540 posterior-middle part of the SC. **c**, A standard deviation projection of calcium responses to
541 moving dots. **d**, Calcium responses of a sample neuron to moving dots and moving bars at
542 twelve directions. Gray shade indicates the standard deviation across identical trials. Small
543 wiggles in the moving dot response reflect individual dots crossing the receptive field.
544 Bottom, polar graphs of normalized peak responses. **e**, Histogram of direction selectivity
545 index of neurons responding to moving dots. Dashed line indicates the threshold applied
546 for direction selectivity analysis. Arrowhead marks the cell in (d). **f**, Histogram of direction
547 selectivity index of neurons responding to moving bars, displayed as in (e).

548 **Figure 2 | Locally uniform direction tuning. a**, All direction-selective neurons in a
549 sample field of view from left SC. Arrows are plotted at the anatomical location of the
550 neurons and indicate the preferred direction in monitor coordinates. Dots are neurons with
551 low direction-selectivity. Dashed lines divide the image into three regions. **b**, Histograms
552 of preferred direction for the three regions. Red lines mark the mean. **c**, A smoothed version
553 of the direction map in (a) where the hue encodes the preferred direction and the intensity
554 varies inversely with the local variance of preferred directions. Note the systematic color
555 gradient across the image. **d**, A 2-D histogram of the absolute difference in preferred
556 directions of two neurons versus their horizontal distance (41 cells, 820 pairs). The red line

557 indicates the mean. (**e**, **f**, **g**, **h**) and (**i**, **j**, **k**, **l**) are single fields of view from two different
558 mice represented in the same way as (**a**, **b**, **c**, **d**) with (88 cells, 382 pairs) and (124 cells,
559 7626 pairs) respectively. The dark regions in **k** indicate large local variance. **m**, The
560 gradient of the map plotted against the absolute difference in preferred directions for pairs
561 within 50 μm for all fields of view (42 images from 14 animals). Blue triangles are from
562 the three sample images in (c), (g), (k). Red star indicates the mean of 1000 samples from
563 a simulated random arrangement of preferred directions; error bar indicates SD. **n**,
564 Histogram of the difference of Bayesian information criterion (BIC) between one-Gaussian
565 and two-Gaussian fitting for all fields of view (42 images from 14 animals). Dashed line
566 indicates the boundary between unimodal and bimodal. Arrows mark the three sample
567 images. Inset, the number of Gaussians that gives the minimal BIC. **o**, Histograms of
568 preferred direction for all direction-selective neurons (n = 2279 cells from 14 animals).

569 **Figure 3 | Direction columns extend in depth. a**, Horizontal plane projection of arrow
570 plots (as in Fig. 2a) at five different depths in the same field of view (229 cells). **b**, 2-D
571 histogram of the absolute difference in the preferred direction versus vertical separation for
572 this volume (236 pairs). Red line indicates mean. **c**, 2-D histogram of the absolute
573 difference in the preferred direction versus vertical separation for all recorded neurons
574 (2323 pairs from 11 animals).

575 **Figure 4 | Direction maps are orthogonal to orientation maps. a**, Calcium responses to
576 moving dots and flashed gratings for a sample neuron exhibiting both direction- and
577 orientation-selectivity. Polar plot shows peak response to dots (blue) and gratings (red).
578 Here the preferred direction and orientation differ by 86°. **b**, Overlay of maps for preferred
579 direction (arrows) and orientation (lines) in a sample field of view, displayed as in Fig. 2a.

580 **c**, Histogram of the absolute difference between preferred direction and preferred
581 orientation for the sample in (b) (60 cells). **d**, Same histogram for all direction- and
582 orientation-selective neurons (532 cells from 14 animals).

583 **Figure 5 | Direction maps from wide-field imaging and two-photon imaging agree. a**
584 **and b**, Direction maps generated from two-photon data and wide-field imaging data in the
585 posterior-medial left superior colliculus of the same mouse. Hue represents the preferred
586 direction (a) and value codes the local variance (a) or the DSI (b). **c**, All direction-selective
587 neurons in the SC of a mutant mouse with undeveloped cortex presented in the anatomy
588 space with preferred direction in monitor coordinates as in Fig. 1a. Dashed line separates
589 images that were acquired with the monitor at two different azimuth coordinates: 95° for
590 the left and 45° for the right. **d**, A smooth direction map from interpolating the data in (c).
591 **e**, Direction map from wide-field imaging data from the same animal as in (d).

592 **Figure 6 | Large-scale direction maps in visual space. a**, Schematic illustrating the
593 correspondence of spherical coordinates and unipolar coordinates. **b**, All direction-
594 selective neurons in the SC of an acortical mouse presented in the visual space using
595 unipolar coordinates. Same recording as Fig. 5c, but the arrows are plotted at receptive
596 field locations. **c**, Direction map obtained from both left and right SC of a different mouse,
597 plotted in visual space with unipolar coordinates. Hue codes the preferred direction; value
598 codes the amplitude of responses; saturation codes the DSI.

599 **Figure 7 | Orientation bias in the direction map. a**, Distribution of preferred directions
600 encountered in both visual hemifields (9 animals). Error bars represent one standard error
601 across animals. Bottom: The histogram for the left hemifield was flipped about the vertical

602 and overlaid on the histogram for the right hemifield. **b**, The radial profile of
603 autocorrelation for a sample direction map. Full-width at half maximum (FWHM) is
604 indicated. **c**, Box plots of the FWHM for the autocorrelation, the cross-correlation between
605 left and right SCs, and the cross-correlation between individuals for the same side of the
606 SC (9 animals). The box plots 25th to 75th quartiles, the band inside the box is the median,
607 and the square inside the box is the mean. The ends of the whisker indicate one standard
608 deviation above and below the mean. **d**, Projections of preferred-direction maps from
609 experimental data onto motion maps representing different optic flows (9 animals). Error
610 bars represent one standard error. Wilcoxon signed-rank test or one-sample *t*-test were
611 applied to test the significance of the difference from 0; the p-values are 1.5e-3, 4.3e-6,
612 3.1e-5, 0.043, 3.9e-3, and 0.14 for the left SC; 0.098, 0.039, 0.027, 0.019, 1.5e-4, and 0.08
613 for the right SC. Mann-Whitney U-test or two-sample *t*-test were applied to test the
614 significance of the difference between left and right SCs, and the p-values are 1.8e-3, 2.2e-
615 6, and 0.022 for the right half figure.

616

617 **Supplementary Figure 1 | Additional examples of arrow plots and smooth maps of**
618 **preferred direction.** Data from 4 animals stimulated with moving dots, presented as in
619 Figs 2a and 2c.

620 **Supplementary Figure 2 | Organization of motion direction measured by moving bars.**
621 (**a**, **b**, **c**, **d**) Data from 4 animals stimulated with moving bars, presented as in Figs 2a and
622 2c. **e**, Gradients of the map plotted against the absolute difference in preferred directions
623 for pairs within 50 μm (33 images), displayed as in Fig. 2m. **f**, Analysis of bimodality in
624 the distributions of preferred direction (33 images), displayed as in Fig. 2n. **g**, Histograms
625 of preferred direction for all direction-selective neurons (1754 cells).

626 **Supplementary Figure 3 | Another sample showing the orthogonal relationship**
627 **between preferred direction and orientation. a.** Overlay of arrow plots for direction-
628 selective neurons and line plots for orientation-selective neurons. **b**, Histogram of the
629 absolute difference between preferred direction and orientation (25 cells).

630 **Supplementary Figure 4 | Introduction of unipolar coordinates. a,** Schematic of the
631 definition of unipolar coordinates (see **Methods**). **b and c**, Relationship between spherical
632 coordinates and unipolar coordinates.

633 **Supplementary Figure 5 | Direction maps including both sides of the SC. a,** A sample
634 direction map plotted in visual space with unipolar coordinates. Hue codes the preferred
635 direction. Value codes the amplitude of responses. Saturation codes the DSI. The horizontal
636 component of the direction in the left field has been flipped to better reveal left-right
637 symmetry. **b**, Average direction map combined over 9 animals.

Supplementary Figure 6 | Autocorrelation and cross-correlation of global direction maps. a. Left, the autocorrelation of a sample direction map. Right, the corresponding radial profile. **b.** Left, the cross-correlation between direction maps of the left and right SCs of an example animal. Right, the corresponding radial profile, centered on the peak of the correlation map. **c.** Left, the cross-correlation between direction maps of the same-side SCs of two different animals. Right, the corresponding radial profile.

Supplementary Figure 7 | Motion maps corresponding to optic flows from self-motion. For each of the 6 basic modes of translation and rotation, this plots the direction of the optic flow vectors in the visual field using unipolar coordinates. Note these graphs assume that the axis of forward translation and roll rotation equals the lambda-bregma axis. In actuality, an ambulating mouse carries the lambda–bregma axis at a typical downward pitch of 29°[43].

Supplementary Figure 8 | Comparison of preferred direction or orientation measured by different stimuli. a. Preferred direction measured by moving bars plotted against that by moving dots (1085 neurons from 14 animals). **b.** Histogram of difference between preferred directions measured by these two stimuli. **c.** Preferred orientation measured by moving bars plotted against that by flashed gratings (680 neurons from 14 animals). **d.** Histogram of difference between preferred orientations measured by these two stimuli.

Supplementary Figure 9 | The global bias of direction map is tuned to the detection of approaching aerial predators. a. Arrow plots of the preferred direction in the SC, averaged over 9 animals, and plotted across the visual field in unipolar coordinates. **b**. The motion vectors in the mouse's visual field produced by an aerial predator approaching at constant height from various directions.

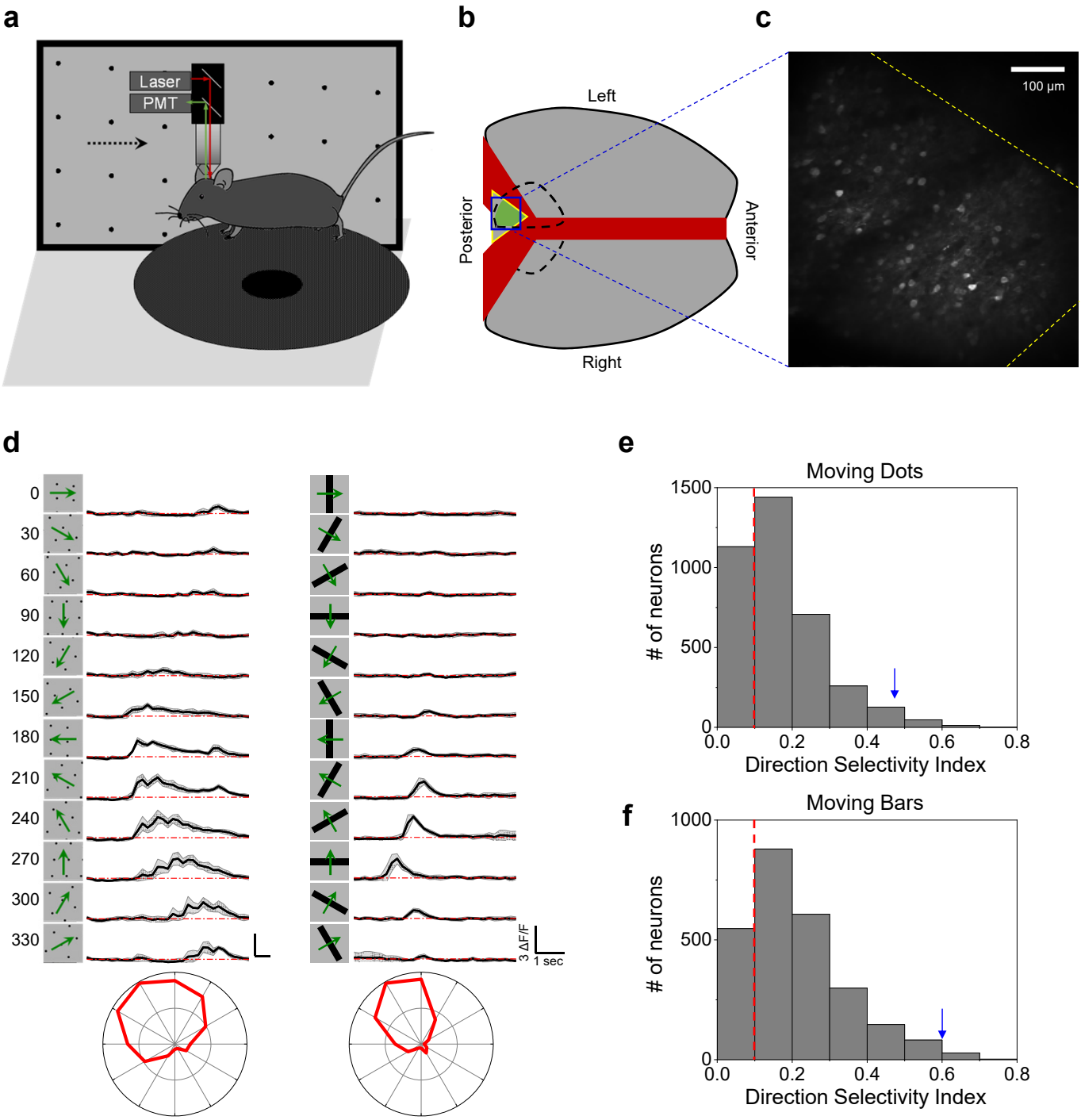
a
Laser
PMT
b
Left
Posterior
Anterior
Right
c
100 µm
d
0
30
60
90
120
150
180
210
240
270
300
330
3 ΔF/F
1 sec
e
Moving Dots
# of neurons
Direction Selectivity Index
f
Moving Bars
# of neurons
Direction Selectivity Index

Figure 1

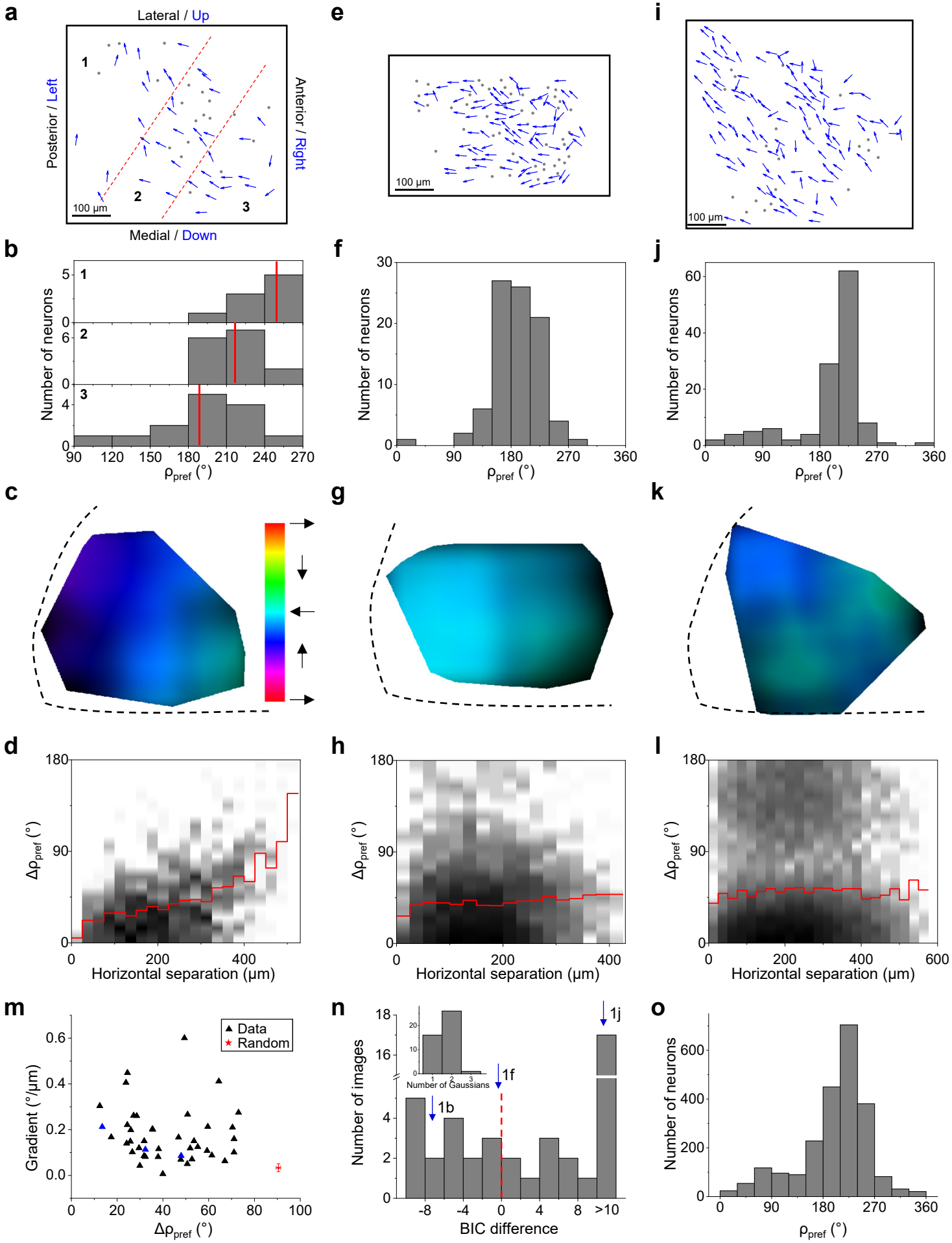
a
Lateral / Up
Posterior / Left
Anterior / Right
Medial / Down
1
2
3
100 µm
b
Number of neurons
ρpref (°)
c
d
Δρpref (°)
Horizontal separation (µm)
e
100 µm
f
g
h
i
100 µm
j
k
l
m
Gradient (°/µm)
Data
Random
n
Number of images
BIC difference
Number of Gaussians
1b
1f
1j
o

Figure 2

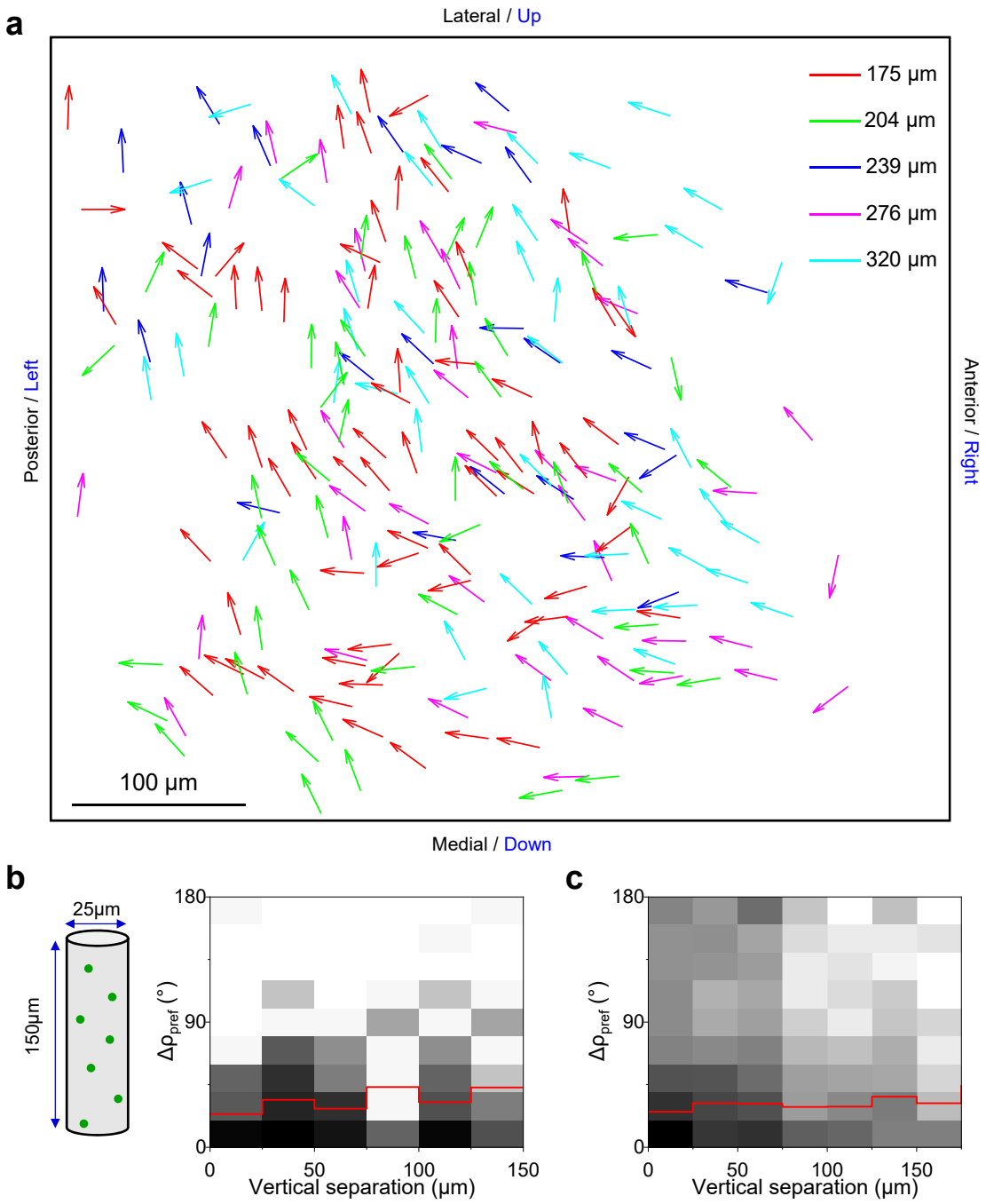
a
Lateral / Up
Medial / Down
Posterior / Left
Anterior / Right
175 µm
204 µm
239 µm
276 µm
320 µm
100 µm
b
25µm
150µm
180
90
0
Δρpref (°)
0
50
100
150
Vertical separation (µm)
c
180
90
0
Δρpref (°)
0
50
100
150
Vertical separation (µm)

Figure 3

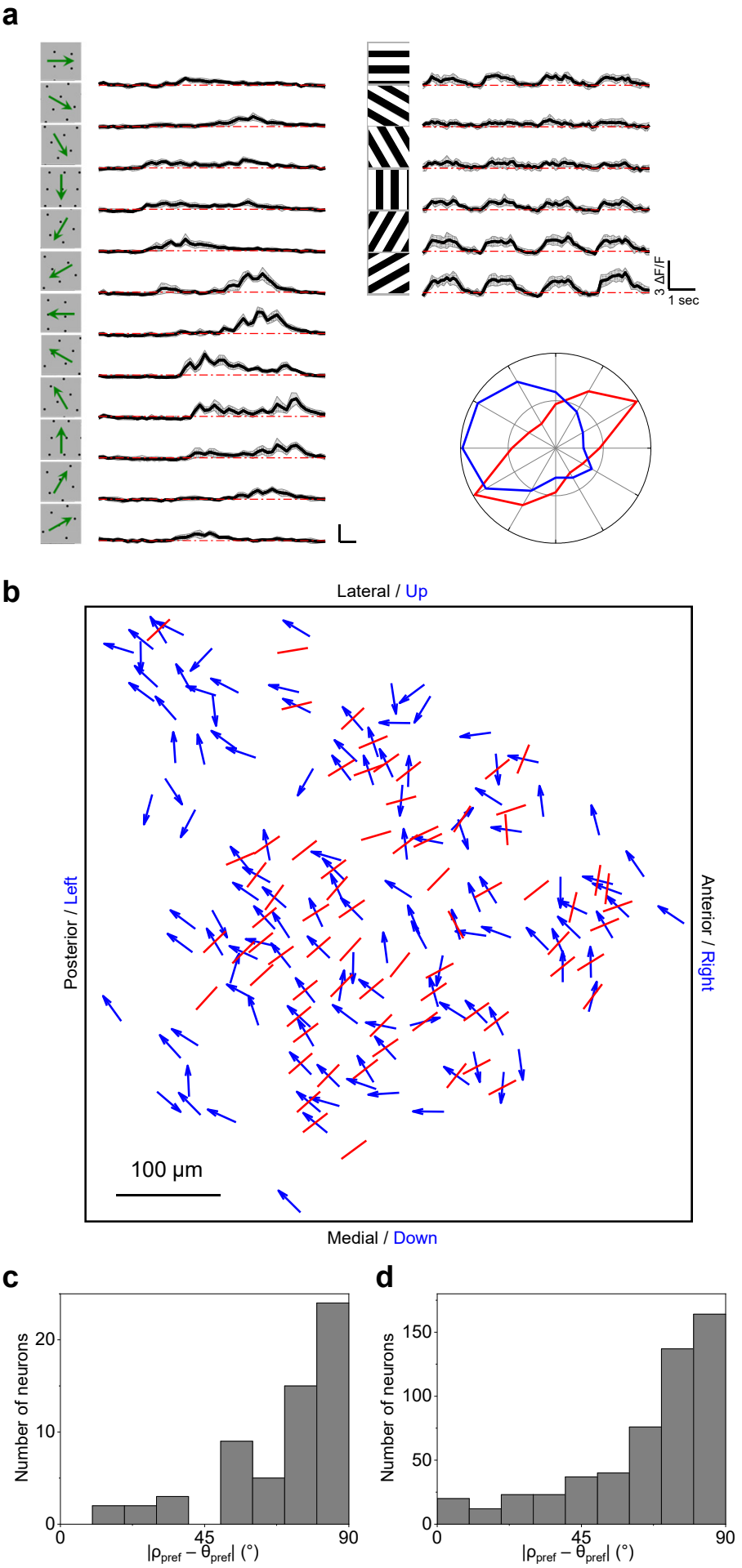
a
3 ΔF/F
1 sec
b
Lateral / Up
Posterior / Left
Anterior / Right
Medial / Down
100 μm
c
Number of neurons
0
10
20
0
45
90
|ρpref − θpref| (°)
d
Number of neurons
0
50
100
150
0
45
90
|ρpref − θpref| (°)

Figure 4

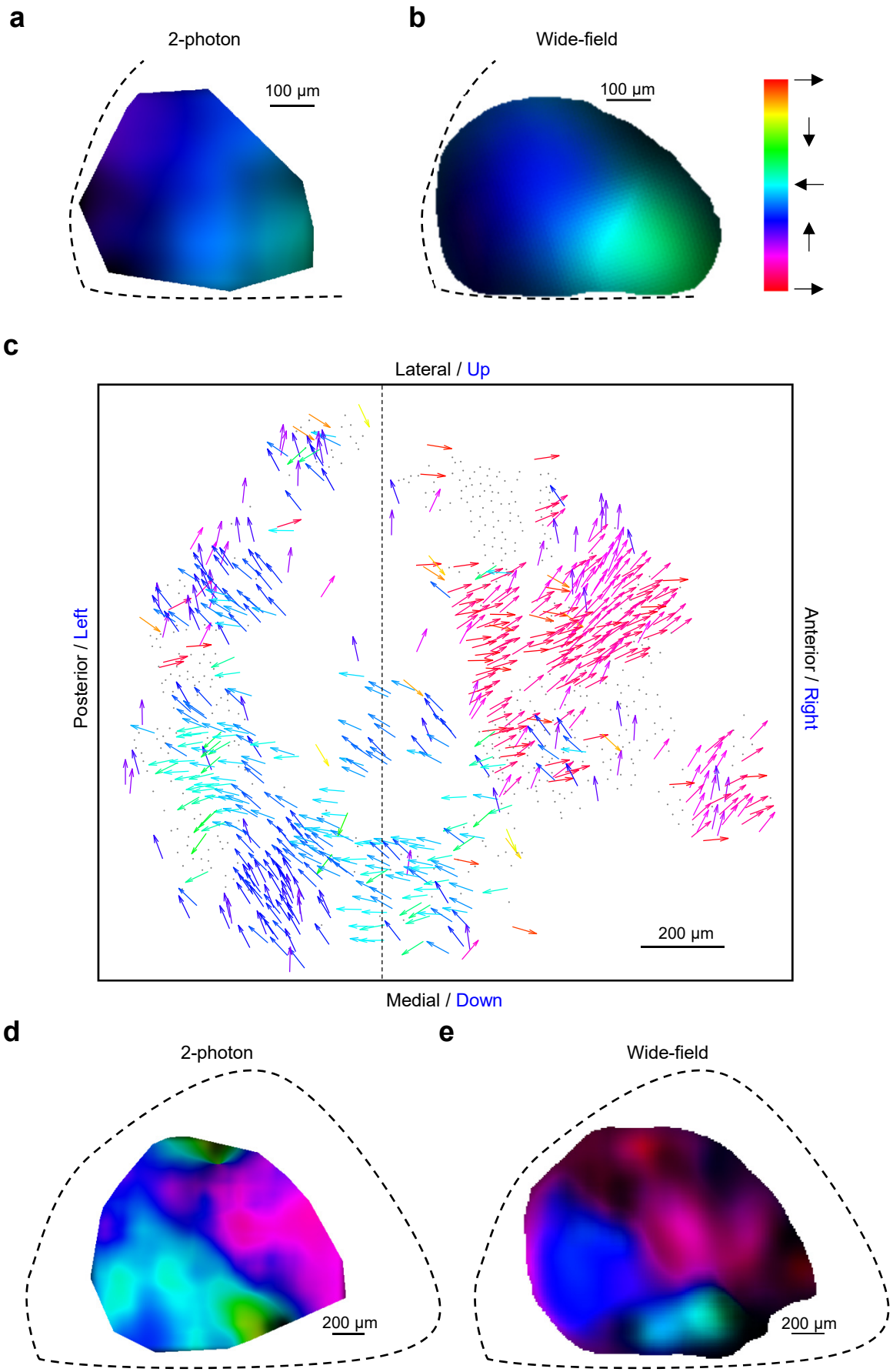
a
2-photon
100 µm
b
Wide-field
100 µm
c
Lateral / Up
Posterior / Left
Anterior / Right
200 µm
Medial / Down
d
2-photon
200 µm
e
Wide-field
200 µm

Figure 5

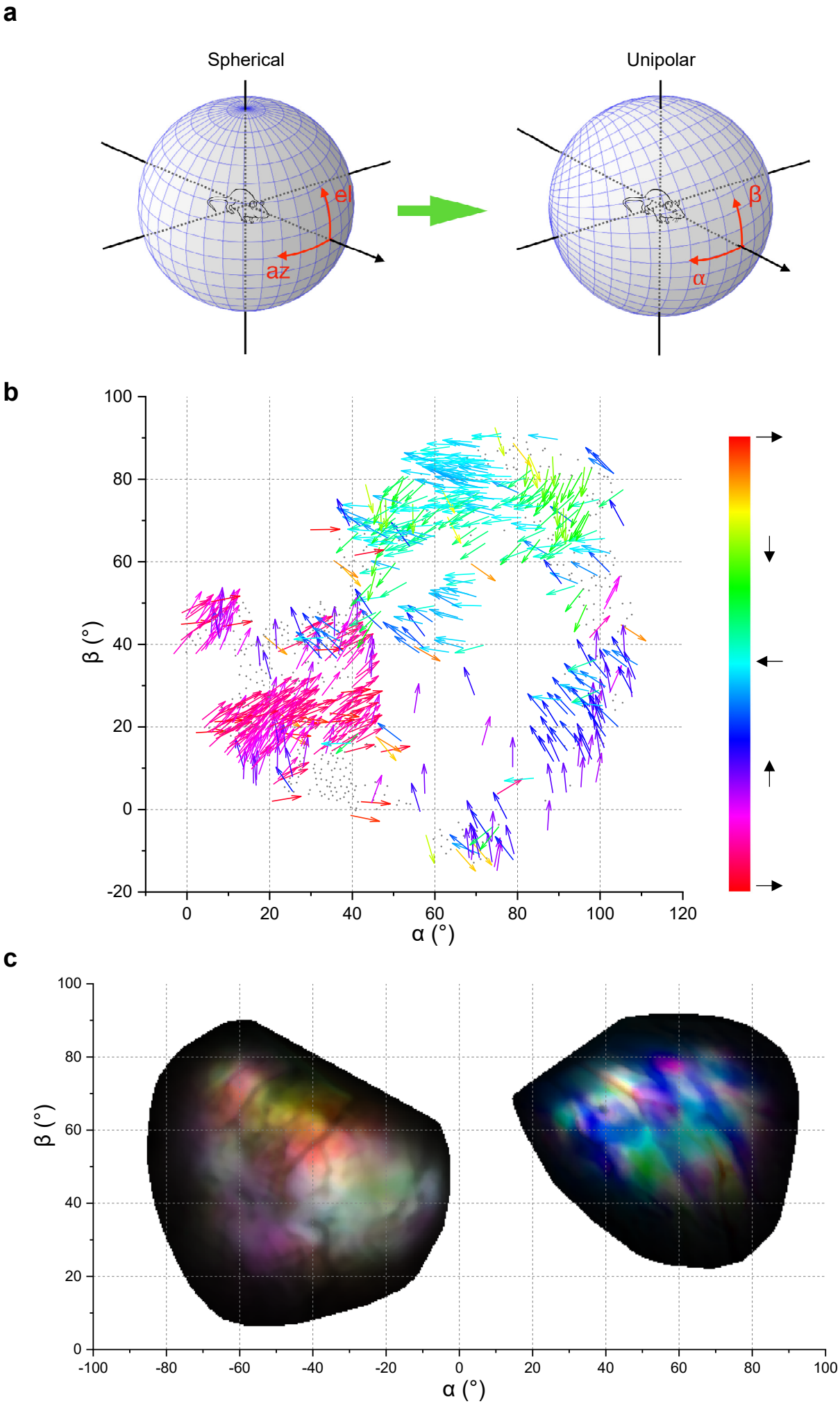

Figure 6

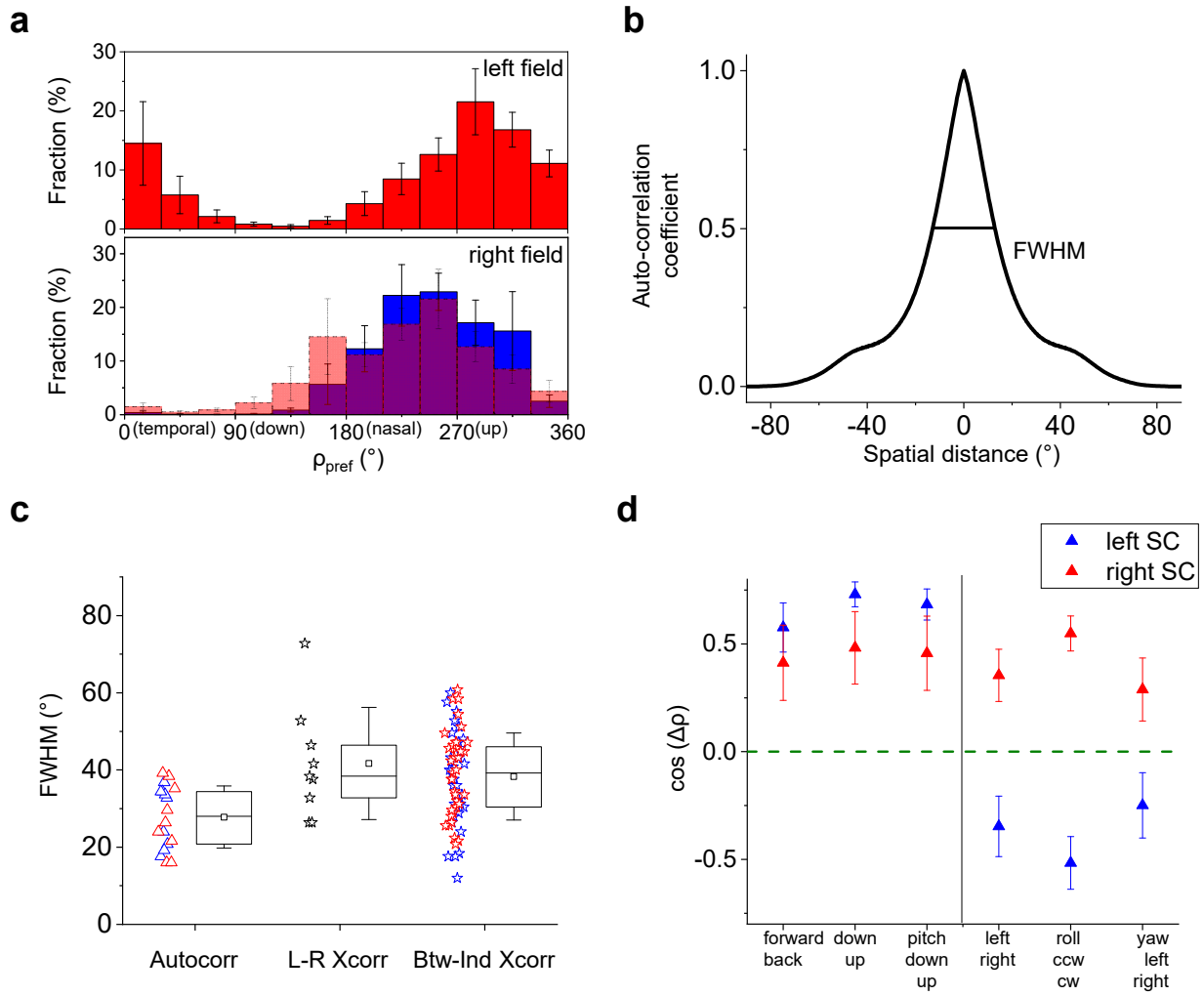
a
left field
right field
Fraction (%)
0 (temporal)
90 (down)
180 (nasal)
270 (up)
360
ρpref (°)
b
Auto-correlation coefficient
FWHM
Spatial distance (°)
c
FWHM (°)
Autocorr
L-R Xcorr
Btw-Ind Xcorr
d
left SC
right SC
cos (Δρ)
forward back
down up
pitch down up
left right
roll ccw cw
yaw left right

Figure 7

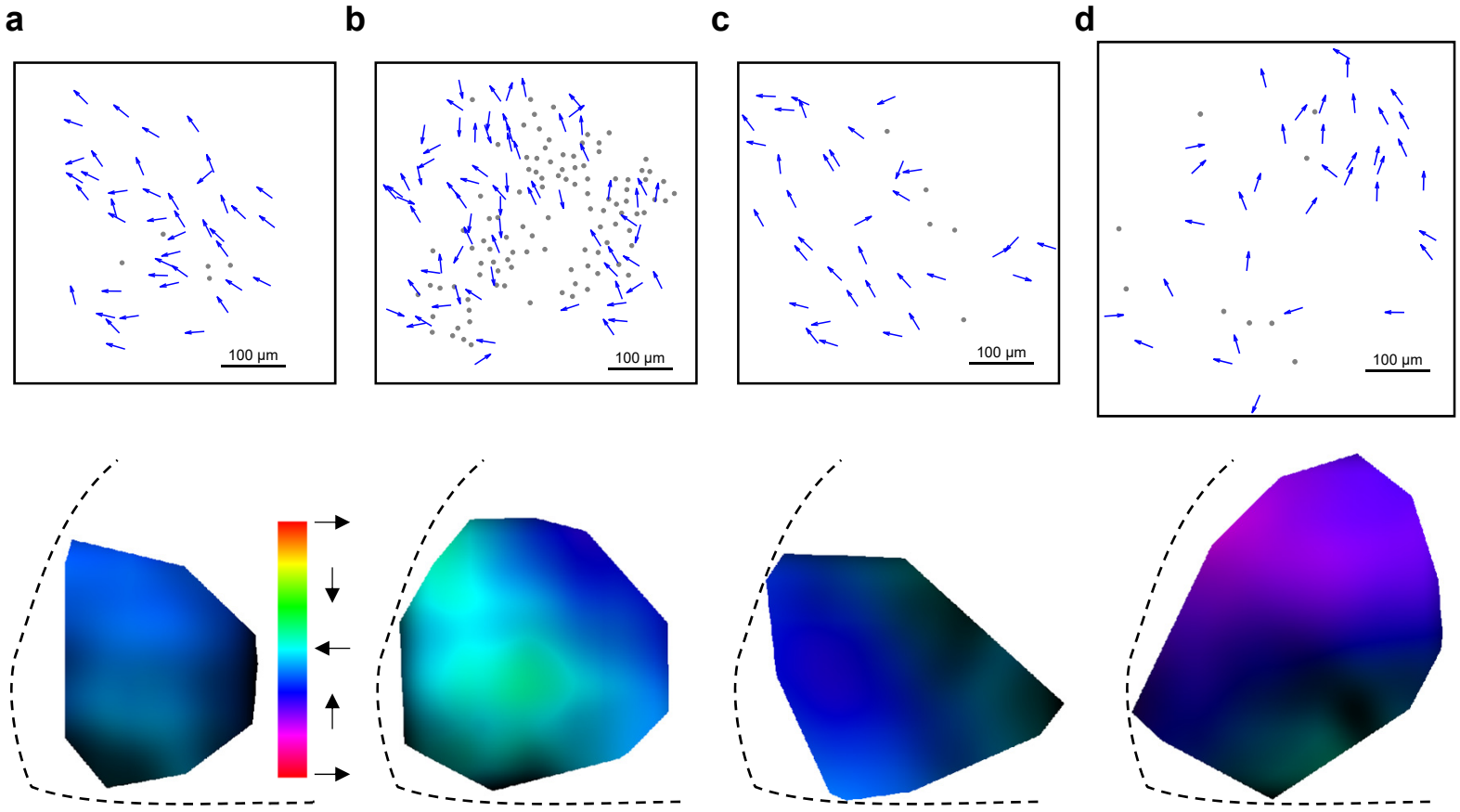

Supplementary Figure 1

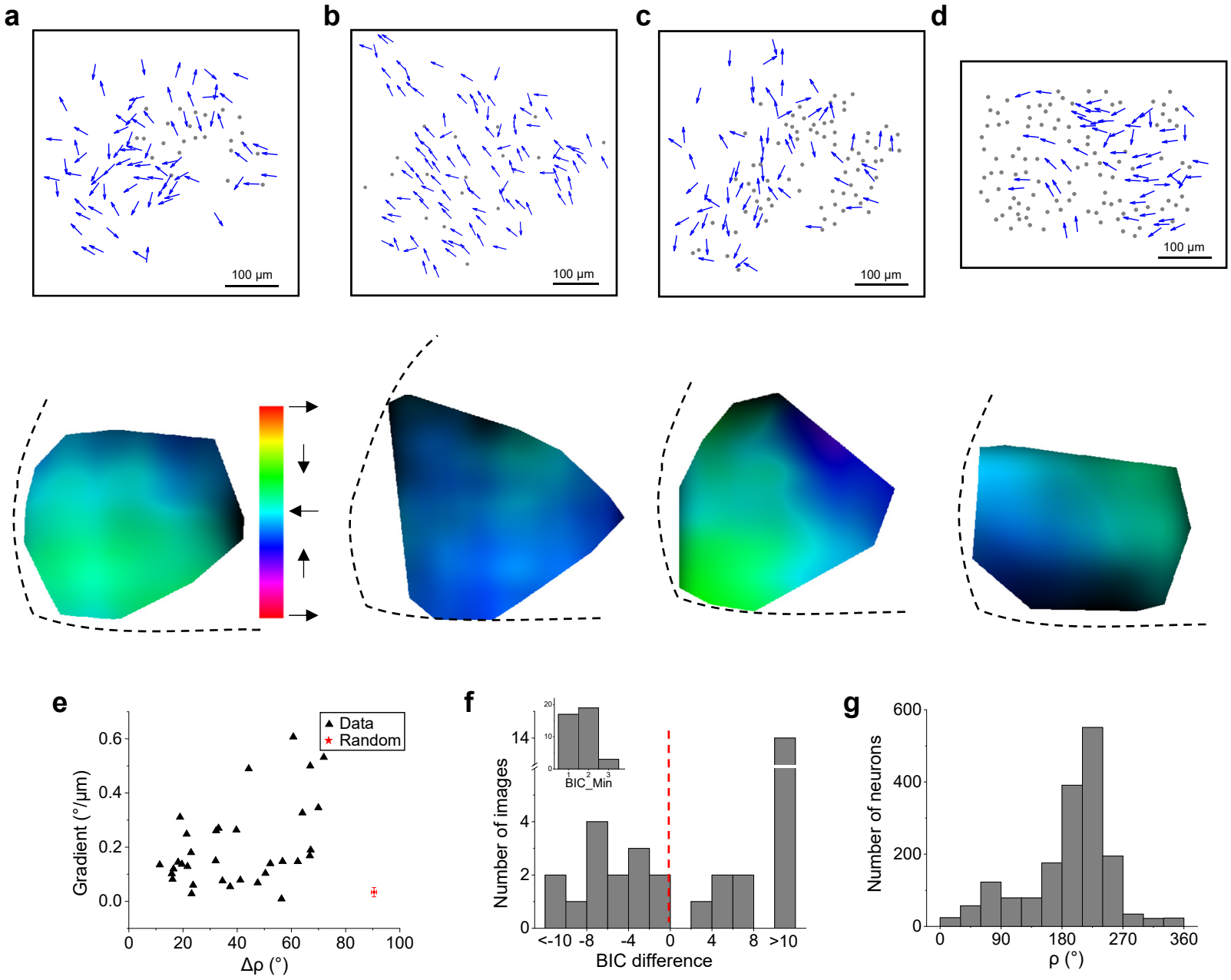

Supplementary Figure 2

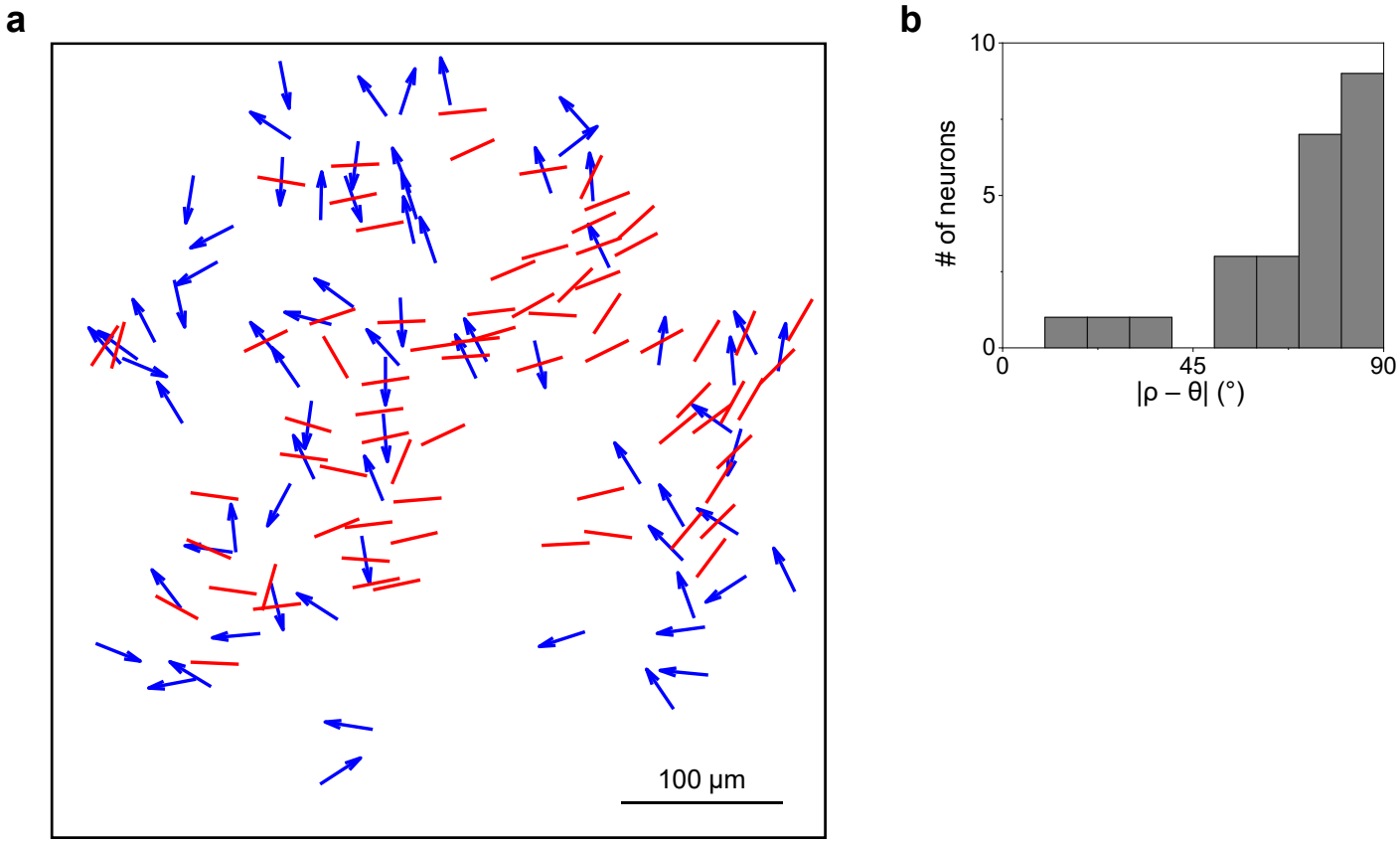

Supplementary Figure 3

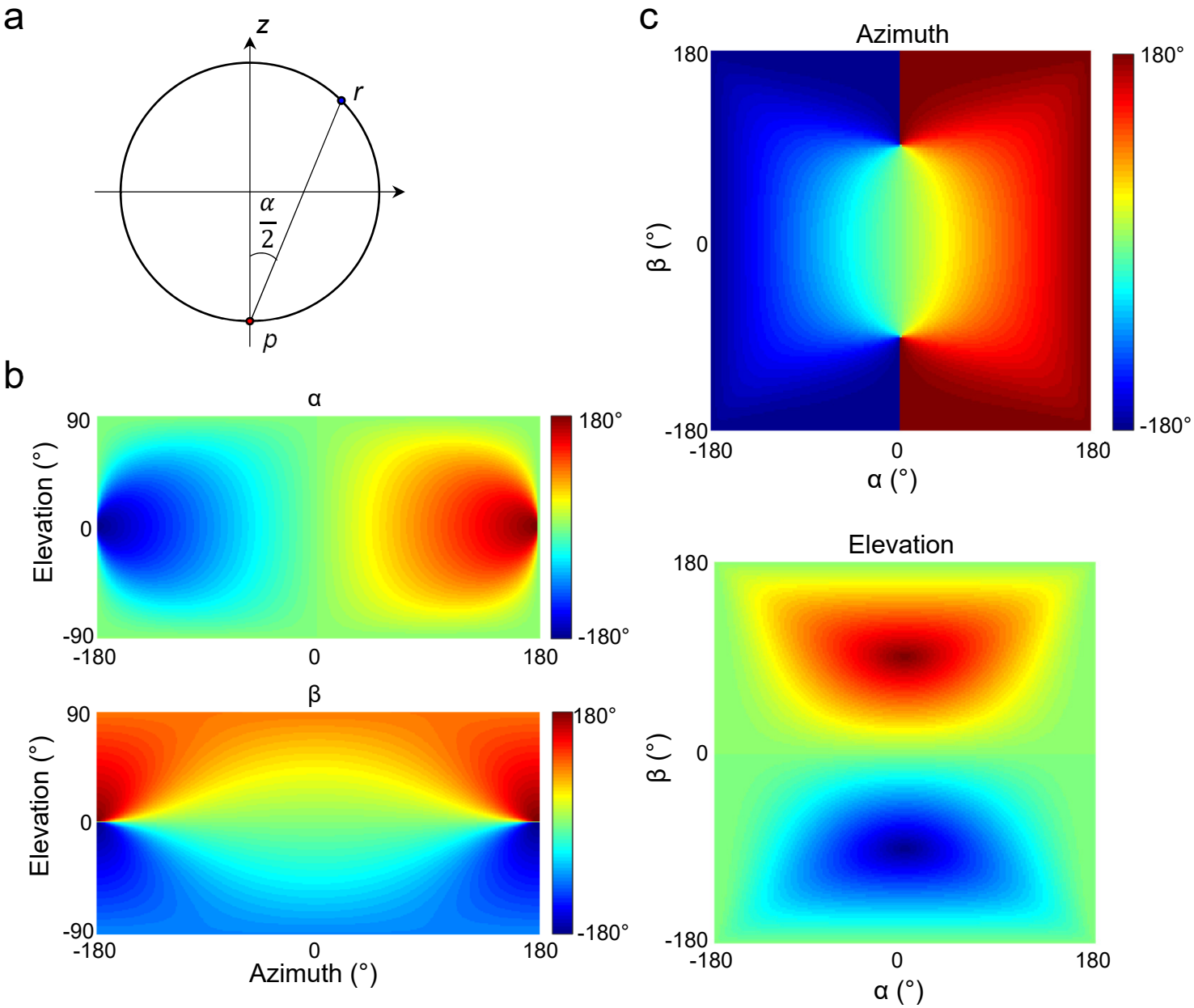

Supplementary Figure 4

a

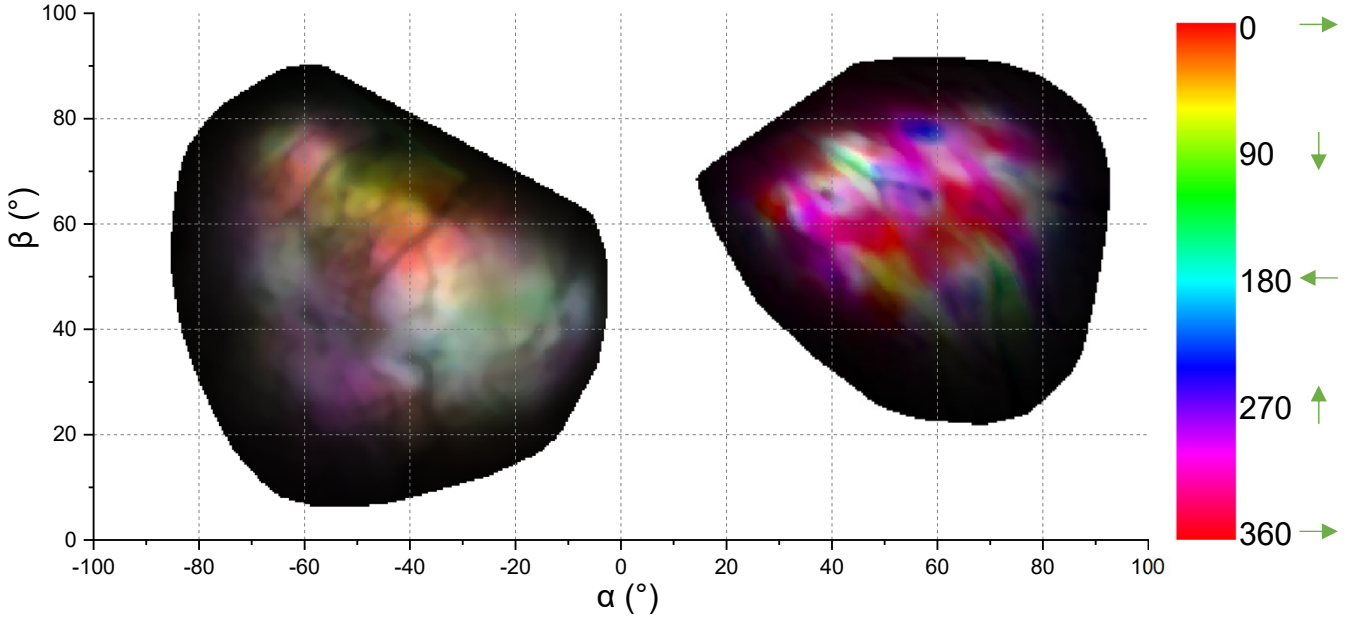

b

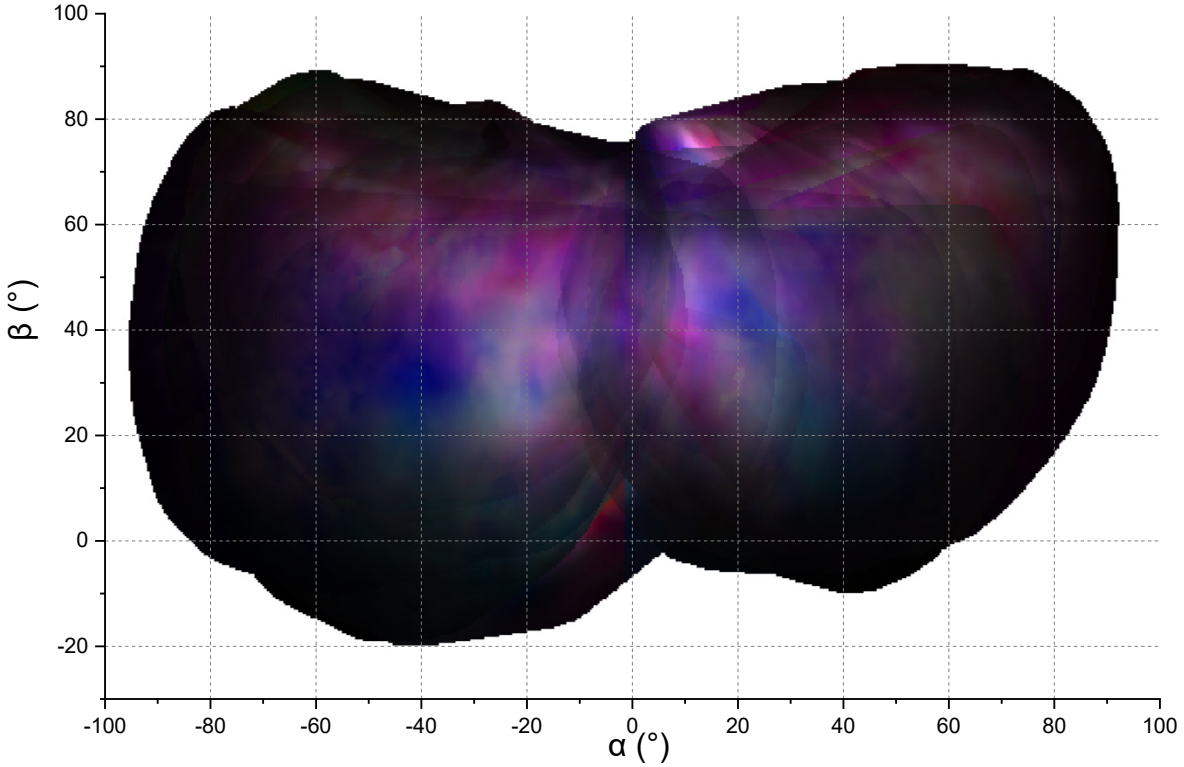

Supplementary Figure 5

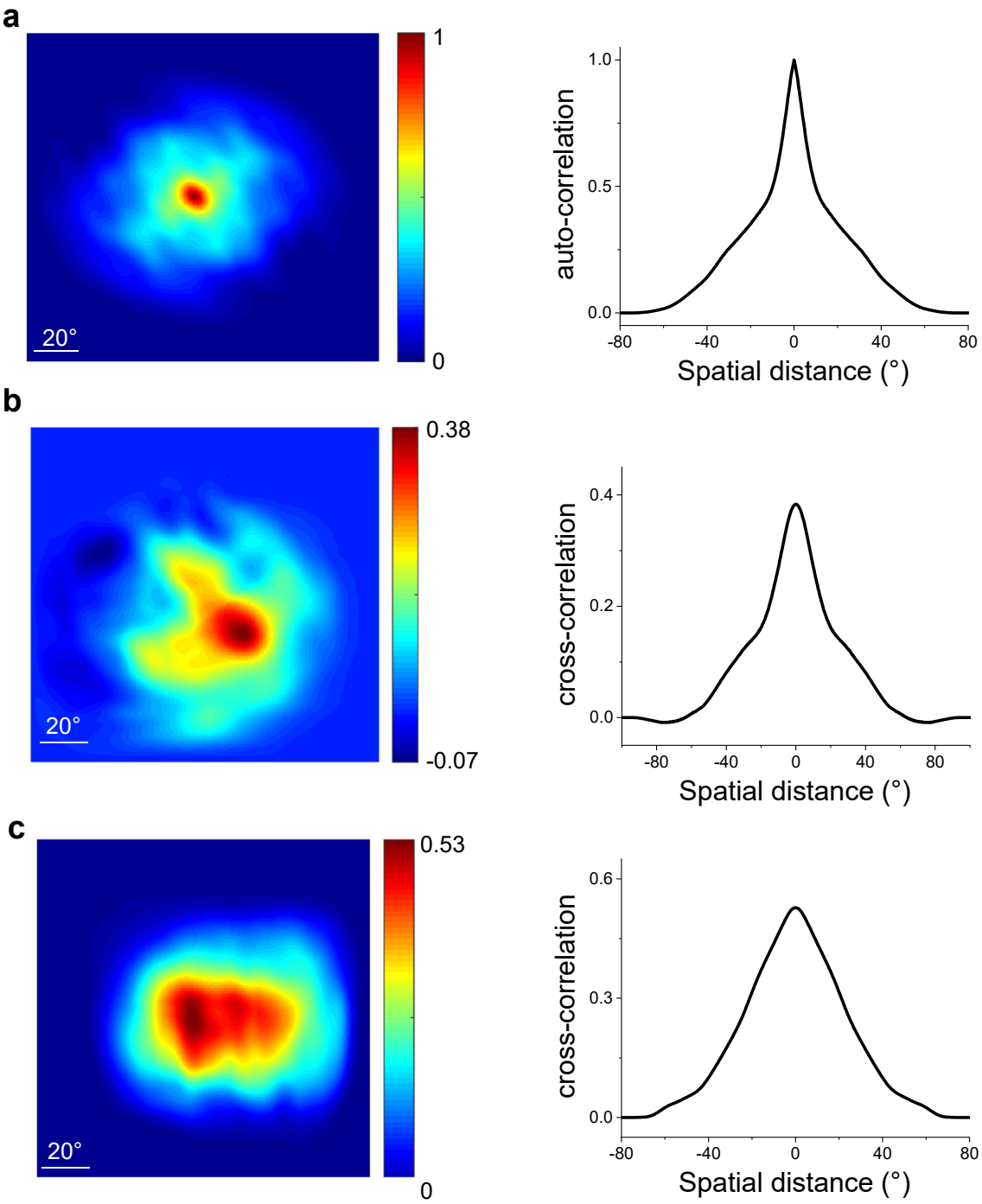

Supplementary Figure 6

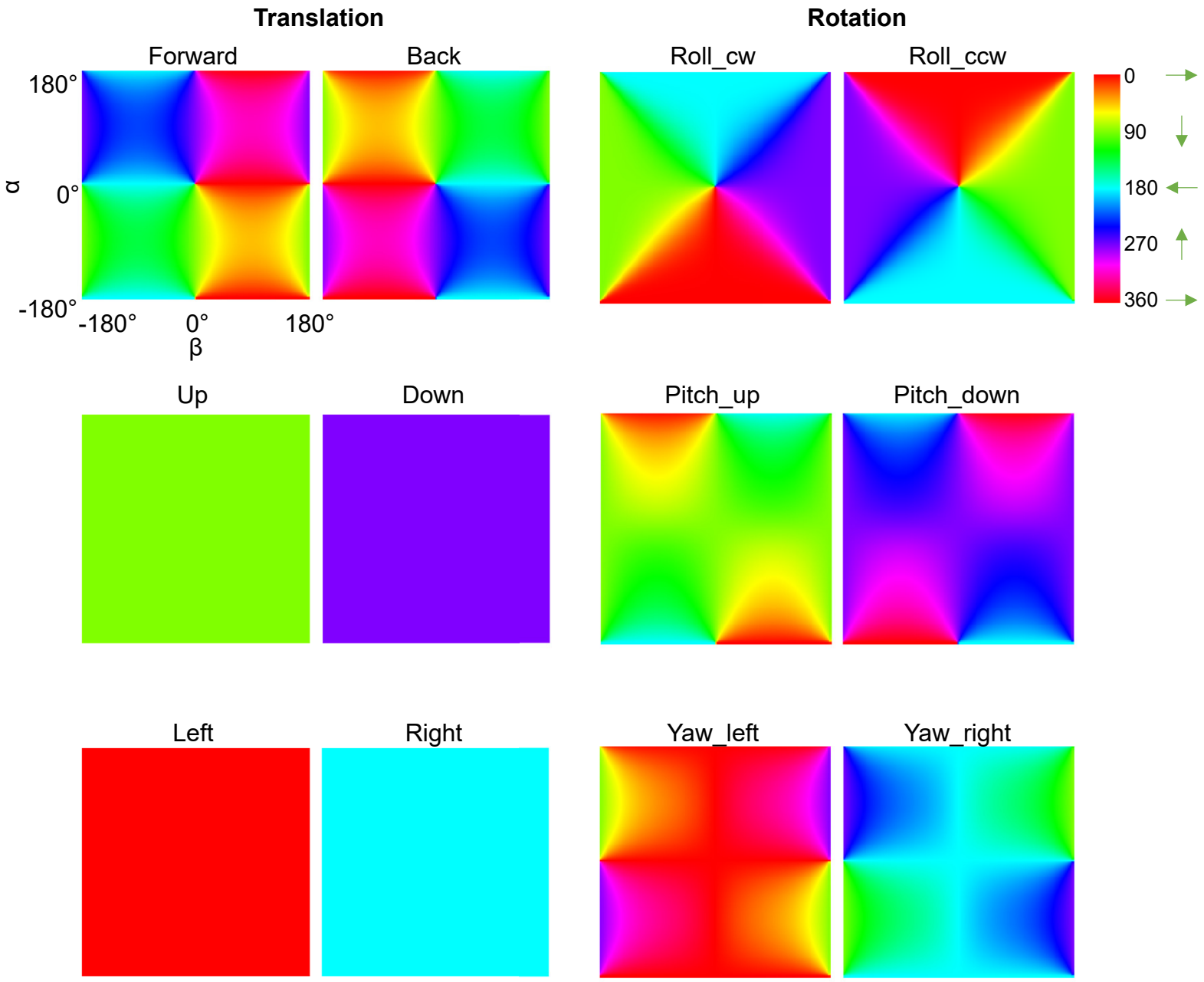

Supplementary Figure 7

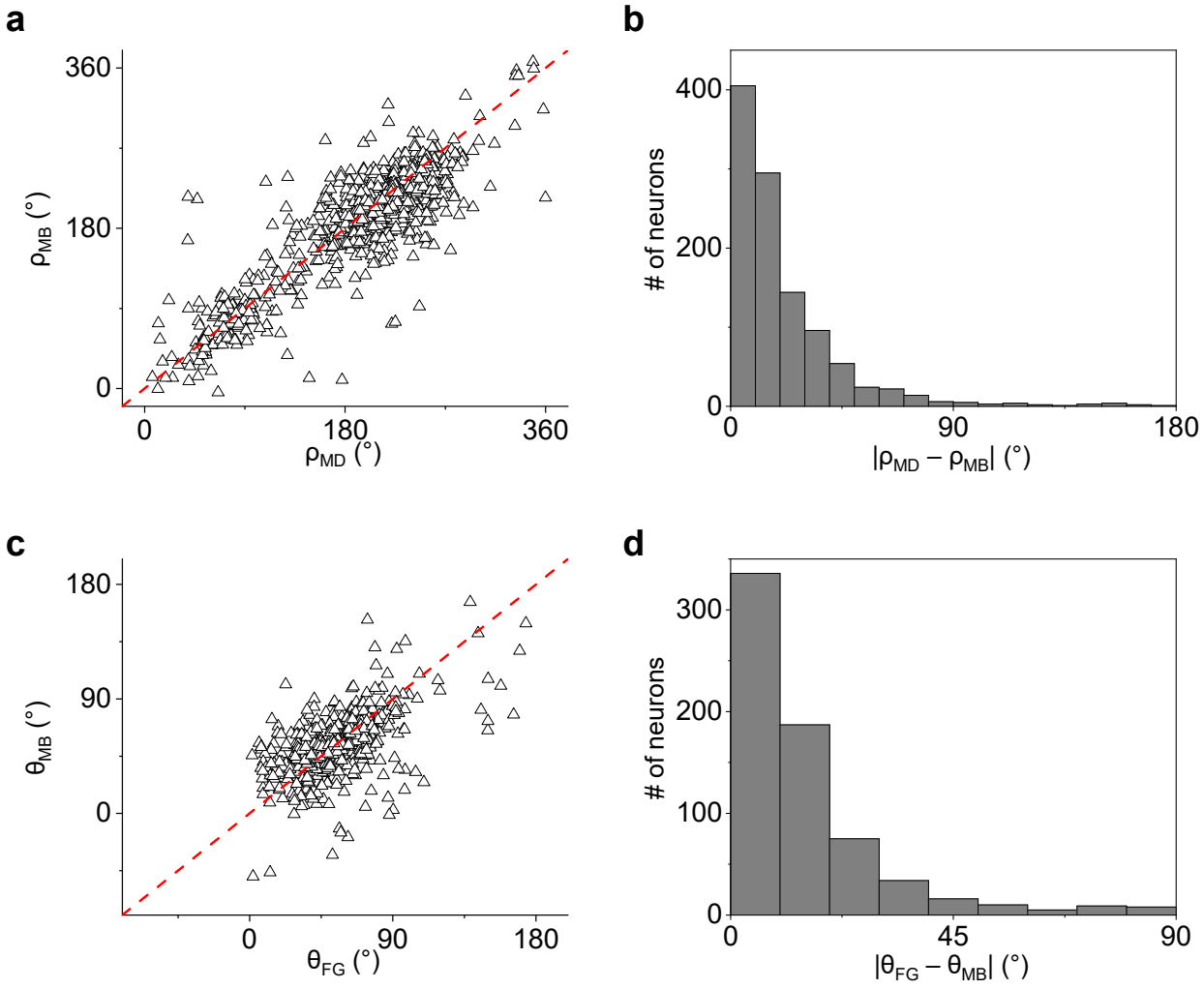

Supplementary Figure 8

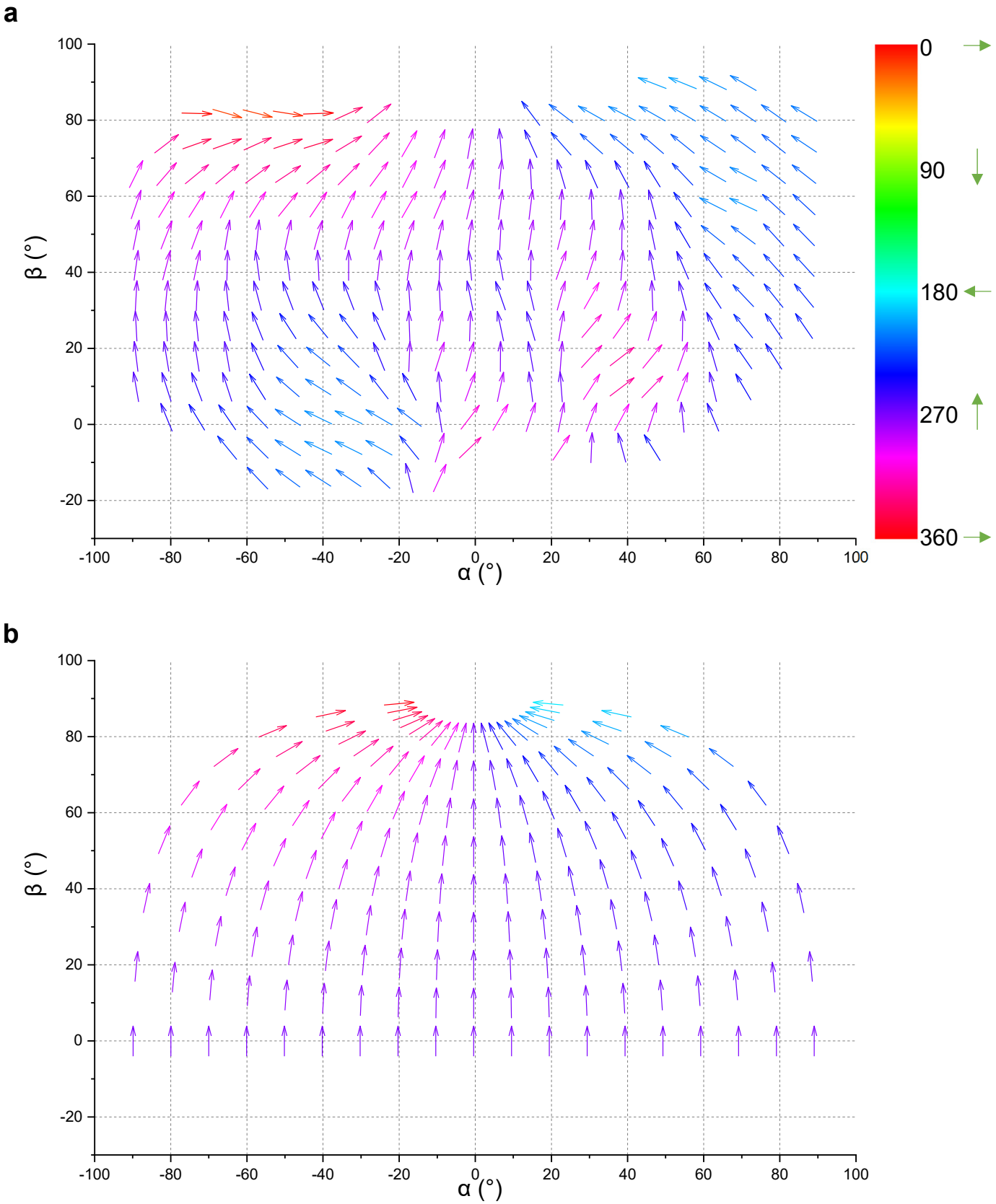

Supplementary Figure 9